
# Nonlinear Finite Element Model of a Geothermal Well

A dissertation by

Lilja Magnúsdóttir

submitted to the Faculty of Industrial Engineering, Mechanical Engineering and Computer Science in partial fulfillment of the requirements for the degree of master of science.

University of Iceland 2009

University of Iceland
Faculty of Industrial Engineering, Mechanical Engineering and Computer Science
VR-II, Hjarðarhaga 2-6, IS-107 Reykjavik, Iceland
Phone +354 525 4000, Fax +354 525 4632
verk@hi.is
www.hi.is

# Abstract

The objective of the study is to make a complete finite element model of a geothermal well. Three casings, cement around the casings, a liner and the formation surrounding the well were modeled with three different types of finite element models. A two dimensional thermal model was used to analyze the temperature distribution of the well and a two dimensional structural model was used to estimate the rise of the production casing along with the well's stress distribution. Finally, a three dimensional buckling model was built to examine the buckling behavior of the production casing where the results from the two dimensional models were used to define loads and constraints.

The maximum upward displacement of the production casing for a 2300 m deep well is 0.05 m according to the two dimensional structural model, but a rise of around 0.13 m has been detected in casings at power plants in Iceland [Gretarsdottir, 2007]. Different contact behavior was defined between the cement and the steel in the production pipe and it greatly affected the results. The stresses were also examined and compared to the yield strengths of the materials. The Von Mises stresses in the steel did not reach the steel's yield stress but the y-component of the compressive stress in the cement reached the ultimate strength of the cement and well over. Different values of the Young's modulus for the cement were also examined in order to estimate its effect on the expansion. The Von Mises stresses were considerably higher when the Young's modulus was increased, but it did not affect the displacement results of the production pipe. When the well was modeled with a three dimensional buckling model, buckling did not occur for the loads defined. However, a load magnitude of 85.3% of the loads defined in the model, caused the well to buckle when a 20 MPa sideward pressure was modeled. The sideward pressure area was increased and the buckling load stayed the same but the displacements where the well buckled were larger for the increased area.

The models built in this project can be useful when designing geothermal wells, to estimate the effects of different properties of the well defined. According to the case study performed, buckling is not unlikely to occur in real geothermal wells and the buckling model could be used to estimate whether changing some parameters would result in decreased risk of failure due to buckling.

# Contents

# List of Tables

# List of Figures

# Acknowledgements

This study was performed under the supervision of dr. Fjóla Jónsdóttir and co-supervised by dr. Halldór Pálsson, both Associate Professors at the Department of Industrial Engineering, Mechanical Engineering and Computer Science at the University of Iceland, and by Sigrún Nanna Karlsdóttir Material Engineer at the Innovation Center Iceland. I dearly thank them for all their assistance and support during the study. I also thank Bjarni Pálsson from Landsvirkjun Power, which was the fourth member of the thesis committee.

The Innovation Center Iceland and Rannís receive my greatest gratitude for sponsoring the work which is a part of the research project "High Temperature Geothermal Wells - Center of Excellence in Iceland". The work is also partly supported by Landsvirkjun and I deeply thank them for their support.

The thesis was improved by communication with many experts on the field of geothermal energy and I owe them many thanks for their advice and contribution to my work.

# 1 Introduction

Geothermal energy is utilized all over the world for electricity production and for heating purposes directly. The major part of geothermal power plants are the wells, usually drilled to depths of 2-3 kilometers into geothermal reservoirs, to gain steam and hot water for the power generation. The wells consist of three steel casings, a liner and cement slurry cemented concentrically between the casings and the surrounding rock. The temperature of the innermost casing reaches high temperatures, as high as 350°C, when the well is brought into production, which results in high thermal stresses [Hammons, 2007]. Under these conditions the casing may easily be in compression hot-yield and a high casing failure risk is often observed in the form of buckling. The drilling and well construction is probably one of the most expensive features of a geothermal direct use project so it is important to reduce the well's risk of failure [Culver, 2005].

The aim of this project was to make a complete finite element model of a geothermal well, where three casings, cement around the casings, a liner and the formation surrounding the well, were modeled. Two dimensional thermal analysis was carried out based on known temperature distributions inside the well and for the rock around it. The results are used in a two dimensional structural analysis where the thermal expansion of the innermost casing due to high temperatures is explored. The temperature results from the thermal analysis are used as loads as well as gravity and pressure distribution inside the well. The connection behavior between the innermost casing and the cement is modeled with contact elements where the maximum contact friction stress between the steel and the cement is defined. In the case study, it was endeavored to have the well defined similar to real high temperature wells, but the main objective was to study how the model responded to different properties of the well, considering the prerequisites assumed. Stresses were examined and compared to the yield strengths of the materials and results for different values of the cement's elastic modulus were explored. Different contact behaviors were also modeled in order to study its effect on the results.

Some assumptions must be made in order to use a two dimensional finite element model to analyze the behavior of a geothermal well. Many conditions exist where the casing is subjected to nonuniform loading, such as cement channels and voids, that could cause buckling of the casing. Those instances are difficult to analyze with a two dimensional model since the buckling shape is not axisymmetric. The body forces can also not vary in the direction of the body thickness in a two dimensional model and the loads may not be applied across the parallel planes bounding the top and bottom surfaces.

A three dimensional model of the well was built to examine the buckling behavior of the well's innermost casing. The thermal load is transferred from the two dimensional thermal analysis, other load components are gravity, pressure distribution inside the well and a sideward pressure. The sideward pressure is used to obtain instability in the well that could result from fluid trapped in the cement outside the casing or inward pressure waves due to the flash zone inside the well, where the liquid flashes into vapor. The computer solving time of the three dimensional model is excessive due to its enormous size and the great number of nodes. The size of the formation was modeled smaller, but the displacements of the nodes on the outer surface of the ground are transferred from the two dimensional analysis to simulate the ground's real behavior. Another possibility in the model for reducing the computer solving time, is to have only contact elements on a small part between the production casing and the surrounding cement and to model the well only down to some specific depth. Displacement constraints from the two dimensional analysis are then used on the bottom of the well to simulate the real buckling behavior of the well.

Several finite element models have been made of geothermal wells in the past in order to study their failures to improve the design of the wells. Gretarsdottir used a two dimensional axisymmetric finite element model to simulate the behavior of a well under operating conditions, where the plane used is parallel to the length of the well [Gretarsdottir, 2007]. Temperatures and stresses were analyzed in the vicinity of the well and the rise of the production casing was estimated due to thermal loads. On the one hand, full bonding was modeled between the casing and the cement which resulted in 0.84 mm maximum rise after 6 hours. Additionally, 6% of the elements in the connection between the steel in the production casing and the cement around were merged together which resulted in much higher maximum rise, 14 mm.

Fleckenstein et al. modeled a two dimensional model of one casing and the surrounding cement [Fleckenstein et al., 2005]. The plane used is perpendicular to the length of the well and in this case the cement is perfectly joined to the casing. The results of this model show that the casing collapse resistance is greatly affected by presence of the cement. A cement channel is also modeled, reaching down the entire length of the well with a $60^{\circ}$ circumferential spread, and it results in a much lower collapse resistance of the casing. Similar model is made in [Shahri, 2005] with the steel/cement interface either fully bounded or unbounded and the results revealed extreme effect of Young's modulus, Poisson's ratio, casing thickness, cement thickness and casing eccentricity on the stress magnitudes of the well. No connection between the cement and the steel is assumed in [Philippacopoulos and Berndt, 2002], where

two casings, a cement and the surrounding formation are modeled. The well is subjected to pressure/thermal loads on the inner and outer radii but the temperature distribution at any section of the well is assumed as uniform and the far-field temperature is also considered as uniform. The heat conduction is therefore essentially one-dimensional and the thermal stress field is axially symmetric. The results demonstrate the inadequacy of geothermal well design based solely on compressive strength, and show that the stresses in the cement are highly sensitive to far field stresses and the relative stiffness between the cement and the formation.

The report, in [Rechard and Schuler, 1983], presents preliminary numerical and theoretical calculations which indicate that if a casing string under axial compression from thermal elongation, with sizable section where no lateral support is provided due to inadequate cement, the string can buckle. The numerical model used thin-walled beam element with circular cross-section and friction gap element from the MARC finite element program, and only a 13-3/8 inch casing 100 diameters long was examined. Complications due to cross-sectional shape changes due to lateral and bending forces were not included and casing instability from internal-external pressure interaction was neglected. The results from those studies mentioned, show that many factors affect the risk of well's failure, and they must be taken into consideration when the wells are designed.

Number of three dimensional finite element models have been made to model geothermal reservoirs but not the well itself like modeled in this project. One model comparable to the model in this project is a localized three dimensional model built by Philippacopoulos and Berndt [Philippacopoulos and Berndt, 2000]. Well casings made of K-55 carbon steel, cement with elastic modulus 14 GPa and a surrounding formation, were modeled with solid finite elements. A complete casing-cement-rock interaction was assumed and the model was employed for axial and shear damage mechanisms. Displacement boundary conditions were imposed at the model to simulate casing shear so it resembles a beam deformed in shear mode. Overburden stress was also applied at the end nodes of the model to account for a depth of 840 feet. The analysis was mainly focused on specific properties of patch cement and their effect on the stresses, and the results indicated a necessity of a patch cement to exhibit tensile capacity when subjected to shear deformations.

In this project, the objective was to make a complete finite element model of the entire well. The model's size is enormous in three dimensions, resulting in high computer solving time but it gives the possibility to model the buckling behavior of the well. There are also many options possible in the model to reduce the computer solving time if the computer resource is not powerful enough. Those possibilities were used in the case study of this project, because the model was limited to the student version of the finite element model ANSYS. The well was therefore only modeled down to 160 m and the radius of the formation modeled was 35 cm, but displacements from the 2d structural model were used as constraints.

The thesis is organized as follows:

Chapter 2 serves as a discussion of geothermal energy in Iceland and worldwide. The construction of geothermal wells is also shown and well failures discussed.

Chapter 3 presents the finite element method. The linear and nonlinear formulations of the finite element method are described, as well as the linear and nonlinear buckling analysis.

Chapter 4 shows the structure of the two dimensional thermal model and the two dimensional structural model.

In Chapter 5 the structure of the three dimensional model is presented. The connection between the two and three dimensional models is also described.

Chapter 6 includes a case study where different types of wells are modeled with both the two and three dimensional models.

Finally, in Chapter 7 the conclusions are summarized and suggestions to further work is described.

# 2 Geothermal Energy and Well Construction

## 2.1 Geothermal Energy

Geothermal energy is the energy extracted from heat stored in the earth which is estimated to be about 5,500 degrees centigrade at the Earth's core [Research, 2008]. The energy is harnessed from underground reservoirs by drilling boreholes into the reservoirs and piping hot water and steam up to a geothermal power plant where it is utilized for heating and power production. The Earth's interior heat is considered abundant and the water used is piped back to the reservoir in most cases, so the geothermal energy is considered to be a renewable resource. The total heat content of the Earth is estimated to be of the order of $12.6 \cdot 10^{24}$ MJ but only a fraction could be utilized by modern technology [Dickson and Fanelli, 2005]. The utilization of the energy is mostly restricted to areas with favorable geological conditions, where heat is carried to or near the surface from deep hot zones.

Geothermal areas can be divided into low-temperature and high-temperature areas based on their geological characteristics. The water temperature in low-temperature areas is 150°C or less at a depth of 1000 meters, but in high-temperature areas the water temperature is 200°C or more at the same depth. The water in low-temperature areas can be used directly for hot water supply because of its low concentration of minerals while the water at higher temperature can not be utilized directly for heating due to dissolved minerals and gases in the water. The high steam pressure and heat content of the water in high-temperature areas are, however, well suitable for generation of electricity and heating up fresh water as a hot water supply [Orkuveita Reykjavíkur].

Around 72 countries reported direct utilization of geothermal energy in May 2005 and the

number of nations using geothermal energy has been growing. The annual compound growth rate was 7.5% from the year 2000 to 2005 and the overall installed thermal capacity was around 28,268 MWt. Iceland is one of the countries with the largest installed capacity and annual energy use, along with USA, Sweden, China and Turkey. Those countries accounted for about 66% of the total installed capacity and 59% of the annual energy use in May 2005 [Lund et al., 2005].

The outermost shell of the Earth, called the lithosphere, is pushed upwards and broken by hot material ascending from the asthenosphere, and it creates what is called the spreading ridges. They are cut perpendicularly by fractures called transform faults and due to the formation of new lithosphere along the ridges and no increase in the Earth's surface with time, a shrinkage of the lithosphere occurs at zones called subduction zones. The lithosphere has been divided into a few major plates based on the subduction zones, transform faults and spreading ridges, as shown in Figure 2.1.

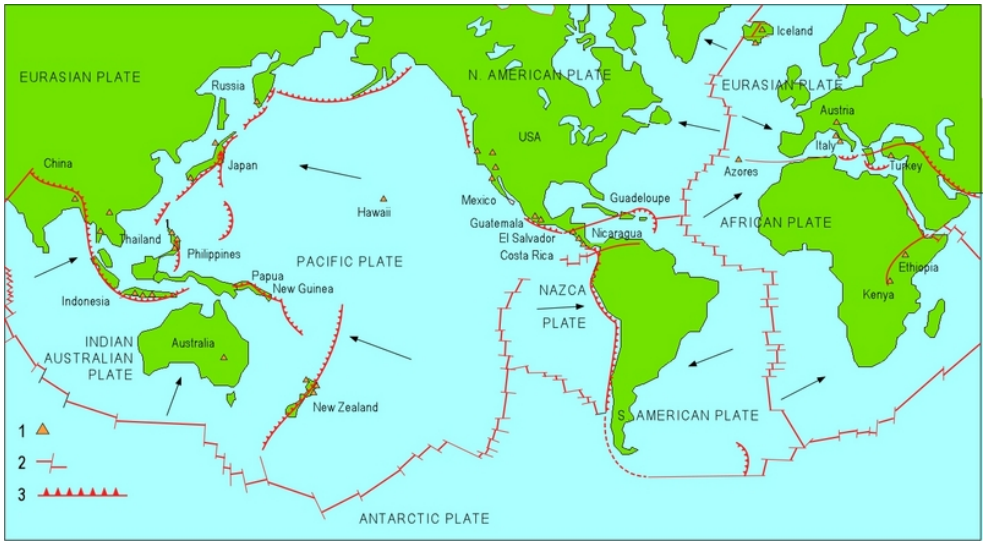


*Figure 2.1: The tectonic plates. 1) Geothermal field producing electricity. 2) Mid-oceanic ridges crossed by transform faults. 3) Subduction zones [Dickson and Fanelli, 2005].*

The terrestrial heat flow is high at the margins of the plates due to the ascent of very hot materials towards the surface, and the most important geothermal areas are located around those margins [Dickson and Fanelli, 2005]. Iceland is situated on the mid Atlantic ridge that forms the boundary between the American plate and the Eurasian plate. Figure 2.2 shows how the active volcanic zone, where the high temperature geothermal resources are located, stretches from the northeast coast of Iceland to the southwest.

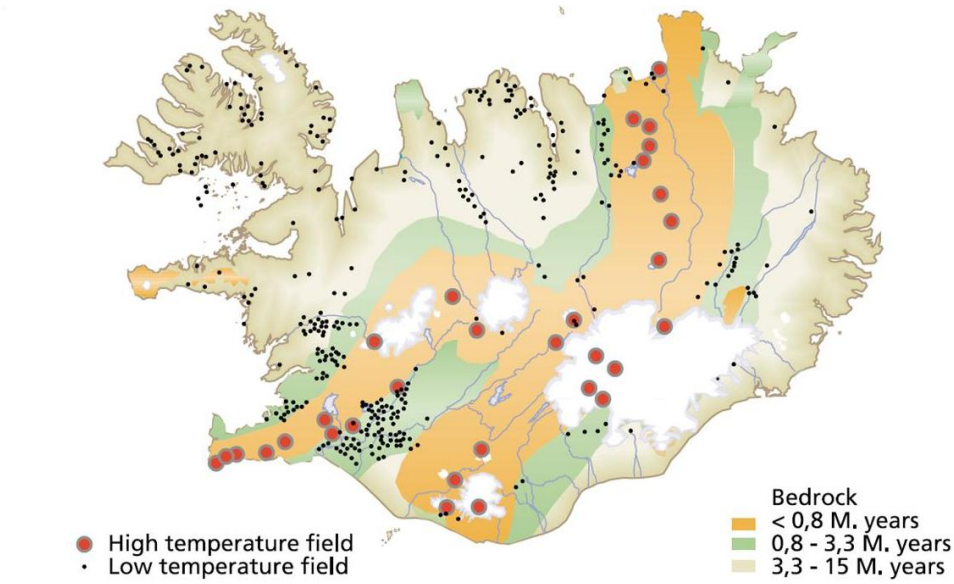


*Figure 2.2: Geothermal map of Iceland [Jóhannesson and Sæmundsson, 2002].*

Geothermal energy pays an important rule in the energy supply of Iceland. In 2006, about 26.5% of electricity generation in Iceland came from geothermal energy but other sources are hydropower and imported fossil fuel [Orkustofnun, 2007].

## 2.2 Geothermal Power Plants

Geothermal powerplants can be combined heat and power plants, i.e. the steam is used not only for electricity generation, but also for heating purposes. Figure 2.3 shows a schematic picture of a combined heat and power plant. Geothermal fluid flows into the wells through holes in the liner and starts to boil, in most cases, on its way up because of a pressure drop in the well. It is gathered into a steam separator where the liquid and steam are separated by reducing the pressure. The wellhead unit consists of the separator and a silencer, which is used to reduce the liquid pressure to atmospheric pressure.

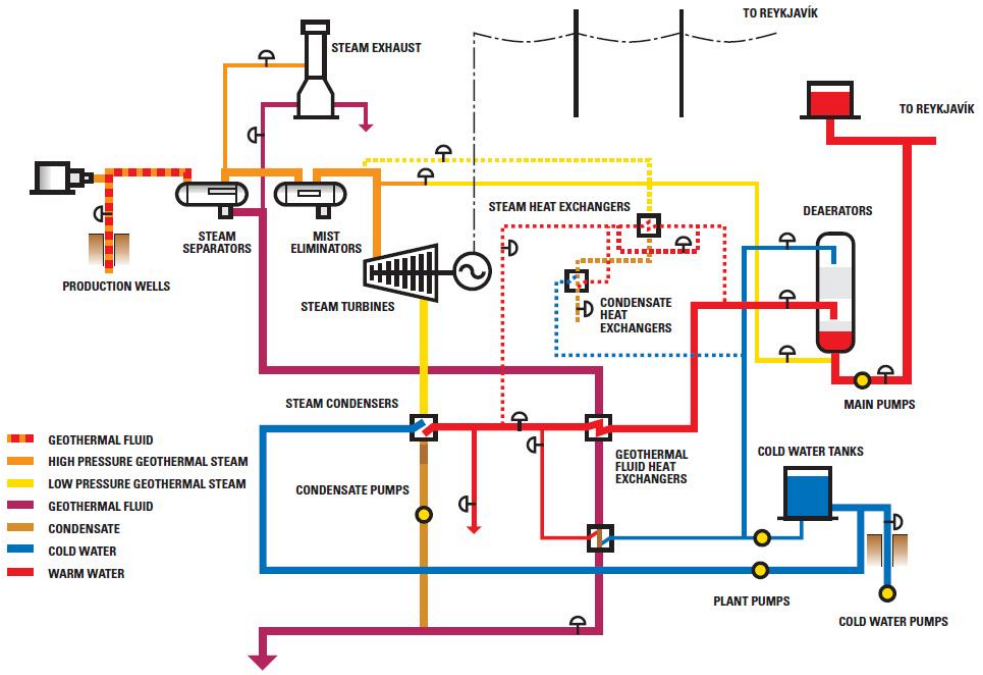


*Figure 2.3: An example of a geothermal power plant's setup [Orkuveita Reykjavíkur, 2003].*

The steam is led into a moisture separator, where any entrained moisture is removed. It is then led through a turbine where it expands and rotates shafts, and converts the geothermal energy into electricity. The steam leaves the turbine as a saturated mixture which is cooled and condensed in a condenser and the back pressure steam is consumed by heat exchangers. Cold fresh water is pumped from shallow wells and it is heated first by the condenser and then by the heat exchanger. The heated water is used for district heating but the mixture from the turbine is injected back to the geothermal reservoir.

## 2.3 Well Configuration and Failures

Geothermal wells are usually drilled to depths of 2-3 kilometers into geothermal reservoirs to gain steam and hot water. A geothermal well is a deep and narrow hole that is cased with steel casings to prevent it from collapsing and to isolate unwanted aquifers. The space between the surrounding rock and the outermost casing is filled with cement slurry, as well as the space between the different types of casings. A typical high temperature geothermal

well consists of a surface casing, an anchor casing, a production casing and a production liner, as can be seen in Figure 2.4.

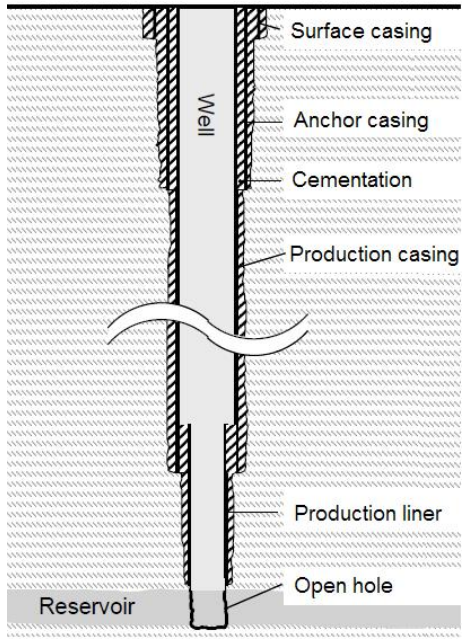


*Figure 2.4: Casings for a high temperature geothermal well (not to scale) [Kaltschmitt et al., 2007].*

The well shown is vertical, as the one modeled in this project, but they can also be directionally drilled. Sometimes it is desirable to drill at an angle to intersect more fractures as well as it can be difficult to locate appropriate drill sites. The proper selection of the type, size and depth of the well casing is based on the expected well operation condition and the drilling site geology. The casings must provide sufficient hole stability, support and protection to aquifers.

It requires advanced technology to harness a high-temperature field for power generation and to drill and design a geothermal well. The temperature of the production casing can reach 200-350°C when the well is brought into production which results in high thermal stresses. Under these conditions the production casing may easily be in compression hot-yield and a high casing failure risk is often observed in the forms of excessive deformation, buckling and collapse. The cost of a typical 2,000 m deep high-temperature geothermal well is approximately US$1.5 million for a vertical well and they are assumed to be one of the most expensive part of a geothermal direct use project. A failure after the well is completed

is likely to result in significant cost of repair and loss of production so it is important to optimize the well's design to reduce the risk of failure [Hammons, 2007].

The risk of well's failure is assumed to increase if fluid is trapped outside the production casing and its thermal expansion causes sideward pressure on the casing. That can occur if there is no or poor cement outside sections of the casing. However, if the casing is well-cemented, the support of the cement may prevent casing failures even though it is hot-yielded and under extreme axial thermal loads [Southon, 2005]. In this project, this defect is simulated in a three dimensional finite element model in order to look into its effect on the casing's buckling strength.

The importance of designing geothermal wells based not only on the compressive strength of the material, but also on the stress fields, nonuniform loadings and interactions between the cement and the steel, has been noticed and the use of the finite element analysis (FEA) method to design casings is gaining wider acceptance with rapidly developing computer softwares and hardware.

# 3 Finite Element Analysis

The finite element method (FEM) is a numerical method used to obtain approximate solutions to partial differential equations that describe a wide variety of engineering problems. The solution approach is based on sup-dividing a complicated domain into series of smaller regions, called elements, in which the differential equations are approximately solved. The elements are connected at specific points referred to as nodes and the process of subdividing is referred to as discretization. At each node the solution is determined in terms of some unknown primary field variables and the degree of freedom (d.o.f.) at that node is the number of those field variables. The values of each field variable (the temperatures, stresses, flows etc.) are assumed to be unknown at the nodal points and the variation within the element can be described in terms of the nodal values by interpolation using functions called shape functions. Those shape functions and the nodal values therefore completely define the behavior of that particular field variable within all the elements.

The updated Lagrangian formulation is used in the commercial finite element program ANSYS for nonlinear analysis to obtain equilibrium equations, using the principle of virtual work [SAS IP, 2007]. The updated Lagrangian formulation refers to the current configuration as a frame of reference, such that stresses and strains are expressed in the current domain of a structure. The equations are linearized at the previously known configuration to yield incremental formulations for nonlinear analysis and, in ANSYS, the Newton-Raphson iterative method is used to solve the nonlinear variational equations.

In this project, a buckling analysis is performed to examine the failure mode of the production casing due to elastic instability. In buckling analysis, the critical loads at which a structure becomes unstable and the buckled mode shape of the structure are determined. There are two buckling techniques available in the ANSYS program, linear eigenvalue buckling analysis and nonlinear buckling analysis. The linear and nonlinear finite element formulation as well as the buckling analysis method will be discussed in the following sections.

## 3.1 Linear Finite Element Formulation

In a linear, elastic range of a homogeneous solid, the relationship between the stresses $\{\sigma\}$ and the strains can be determined using Hooke's law

$$\{\sigma\} = [D]\{\varepsilon^{el}\} \tag{3.1}$$

where $[D]$ is symmetric and referred to as the elastic stiffness matrix. $\{\varepsilon^{el}\}$ is the elastic strain vector, i.e. the strains that cause the stresses, defined by $\{\varepsilon^{el}\} = \{\varepsilon\} - \{\varepsilon^{th}\}$ where $\{\varepsilon\}$ is the total strain vector and $\{\varepsilon^{th}\}$ is the thermal strain vector

$$\{\varepsilon^{th}\} = \triangle T \begin{bmatrix} \alpha_x & \alpha_y & \alpha_z & 0 & 0 & 0 \end{bmatrix}^T \tag{3.2}$$

$\alpha_x$ is the coefficient of thermal expansion in the x direction and $\triangle T = T - T_{ref}$ where T is the current temperature and $T_{ref}$ is the reference temperature [SAS IP, 2007].

The elastic strain can be defined with the vector

$$\{\varepsilon^{el}\} = \begin{bmatrix} \varepsilon_x^{el} & \varepsilon_y^{el} & \varepsilon_z^{el} & \varepsilon_{xy}^{el} & \varepsilon_{yz}^{el} & \varepsilon_{zx}^{el} & \gamma_{xy}^{el} & \gamma_{xz}^{el} & \gamma_{yz}^{el} \end{bmatrix}^T \tag{3.3}$$

where

$$\begin{aligned}
\varepsilon_x^{el} &= \frac{\partial u}{\partial x} + 1/2\left(\frac{\partial u}{\partial x}^2 + \frac{\partial v}{\partial x}^2 + \frac{\partial w}{\partial x}^2\right) \\
\varepsilon_y^{el} &= \frac{\partial u}{\partial y} + 1/2\left(\frac{\partial u}{\partial y}^2 + \frac{\partial v}{\partial y}^2 + \frac{\partial w}{\partial y}^2\right) \\
\varepsilon_z^{el} &= \frac{\partial u}{\partial z} + 1/2\left(\frac{\partial u}{\partial z}^2 + \frac{\partial v}{\partial z}^2 + \frac{\partial w}{\partial z}^2\right) \\
\varepsilon_{xy}^{el} &= 1/2\left(\frac{\partial v}{\partial x} + \frac{\partial u}{\partial y} + \left(\frac{\partial u}{\partial x}\frac{\partial u}{\partial y} + \frac{\partial v}{\partial x}\frac{\partial v}{\partial y} + \frac{\partial w}{\partial x}\frac{\partial w}{\partial y}\right)\right) \\
\varepsilon_{xz}^{el} &= 1/2\left(\frac{\partial w}{\partial x} + \frac{\partial u}{\partial z} + \left(\frac{\partial u}{\partial x}\frac{\partial u}{\partial z} + \frac{\partial v}{\partial x}\frac{\partial v}{\partial z} + \frac{\partial w}{\partial x}\frac{\partial w}{\partial z}\right)\right) \\
\varepsilon_{yz}^{el} &= 1/2\left(\frac{\partial w}{\partial y} + \frac{\partial v}{\partial z} + \left(\frac{\partial u}{\partial y}\frac{\partial u}{\partial z} + \frac{\partial v}{\partial y}\frac{\partial v}{\partial z} + \frac{\partial w}{\partial y}\frac{\partial w}{\partial z}\right)\right)
\end{aligned} \tag{3.4}$$

If the Green strain tensor is used, the strain is defined as a first degree partial derivative of the displacement vector,

$$\varepsilon_{ij}^{el} = \frac{1}{2}(u_{i,j} + u_{j,i} + u_{l,i}u_{l,j}) \tag{3.5}$$

where $u_{i,j} = \frac{\delta u_j}{\delta x_i}$ and the definition of the shear strains is given by

$$\gamma_{ij}^{el} = 2\varepsilon_{ij}^{el}(i \neq j) \tag{3.6}$$

The deformations in structures are in many cases small enough that the quadratic terms in equation (3.4) make no significant contribution so neglecting these terms is justified [Pilkey and Wunderlich, 1994].

In the case of an element of linear and isotropic material, i.e. material properties at a point are independent of orientation, equation (3.1) can be expressed as,

$$\begin{bmatrix} \sigma_x \\ \sigma_y \\ \sigma_z \\ \tau_{xy} \\ \tau_{xz} \\ \tau_{yz} \end{bmatrix} = \frac{E}{(1+\nu)(1-2\nu)} \begin{bmatrix} 1-\nu & \nu & \nu & 0 & 0 & 0 \\ \nu & 1-\nu & \nu & 0 & 0 & 0 \\ \nu & \nu & 1-\nu & 0 & 0 & 0 \\ 0 & 0 & 0 & \frac{1-2\nu}{2} & 0 & 0 \\ 0 & 0 & 0 & 0 & \frac{1-2\nu}{2} & 0 \\ 0 & 0 & 0 & 0 & 0 & \frac{1-2\nu}{2} \end{bmatrix} \begin{bmatrix} \varepsilon_x^{el} \\ \varepsilon_y^{el} \\ \varepsilon_z^{el} \\ \gamma_{xy}^{el} \\ \gamma_{xz}^{el} \\ \gamma_{yz}^{el} \end{bmatrix} \tag{3.7}$$

where $E$ is the modulus of elasticity, called Young's modulus, and $\nu$ is a material constant referred to as Poisson's ratio [Pilkey and Wunderlich, 1994].

The displacement vector of a general point $\{w\} = \begin{bmatrix} w_x & w_y & w_z \end{bmatrix}^T$ describes the displacement within the element and it can be written as,

$$\{w\} = [N]\{u\} \tag{3.8}$$

where $[N]$ is a matrix of shape functions and $u$ is the nodal displacement vector. The shape functions must satisfy two key requirements to ensure convergence to the correct result, completeness and compatibility. The functions should be able to represent the true displacement distribution as closely as possible and they must be continuous [Zienkiewicz, 1977].

If the differentiation of the shape functions is written as,

$$[B] = \begin{bmatrix} \partial_x & 0 & 0 \\ 0 & \partial_y & 0 \\ 0 & 0 & \partial_z \\ \partial_y & \partial_x & 0 \\ \partial_z & 0 & \partial_x \\ 0 & \partial_z & \partial_y \end{bmatrix} \tag{3.9}$$

then according to equation (3.5), the strains may be related to the nodal displacements by

$$\{\varepsilon\} = [B]\{u\} \tag{3.10}$$

The finite element method can be formulated as an energy method. The principle of virtual work states that a virtual change of the internal strain energy $\delta U$ must be offset by an identical change in the external work done on the body by the applied forces $\delta W$, or

$$\delta U = \delta W \tag{3.11}$$

The virtual internal strain energy for a solid region of volume $V$ can be expressed as

$$\delta U_1 = \int_V \{\delta\varepsilon\}^T \{\sigma\} dV^T \tag{3.12}$$

Combining equations (3.1), (3.10) and (3.12) gives

$$\delta U_1 = \{\delta u\}^T \int_V [B]^T [D][B] dV \{u\} - \{\delta u\}^T \int_V [B]^T [D]\{\varepsilon^{th}\} dV \tag{3.13}$$

The following equation shows another form of virtual strain energy, when a surface moves against a distributed resistance as in a foundation stiffness,

$$\delta U_2 = \int_{A_f} \{\delta w_n\}^T \{\sigma\} dA_f \tag{3.14}$$

where $A_f$ is the area of the distributed resistance, $\{w_n\}$ is the motion normal to the surface

and $\{\sigma\}$ is the stress carried by the surface. Combining equations (3.14) and (3.8) gives

$$\delta U_2 = \{\delta u\}^{T_k} \int_{A_f} [N_n]^T [N_n] dA_f \{u\} \tag{3.15}$$

where $[N_n]$ is the matrix of shape functions for normal motions at the surface and k represents the foundation stiffness so that $\{\sigma\} = k\{w_n\}$.

The inertial effects of the external virtual work can be written as

$$\delta W_1 = -\int_V \{\delta w\}^T \frac{\{F^a\}}{V} dV \tag{3.16}$$

where $\{F^a\}$ is the acceleration force vector and according to Newton's second law it can be written as $\frac{\{F^a\}}{V} = \rho \frac{\delta^2}{\delta t^2}\{w\}$ where $\rho$ is the density and t is the time. If the density is constant over the volume, equation (3.16) becomes

$$\delta W_1 = -\{\delta u\}^T \rho \int_V [N]^T [N] dV \frac{\delta^2}{\delta t^2}\{u\} \tag{3.17}$$

The pressure vector $\{P\}$ applied to area $A_p$ can be accounted for by

$$\delta W_2 = \{\delta u\}^T \int_{A_p} [N_n]\{P\} dA_p \tag{3.18}$$

and the nodal forces $\{F_e^{nd}\}$ applied to the element can be accounted for by

$$\delta W_3 = \{\delta u\}^T \{F_e^{nd}\} \tag{3.19}$$

Then equation (3.11) can be written as,

$$\begin{aligned} \{\delta u\}^T \int_V [B]^T [D][B] dV \{u\} - \{\delta u\}^T \int_V [B]^T [D]\{\varepsilon^{th}\} dV \\ +\{\delta u\}^{T_k} \int_{A_f} [N_n]^T [N_n] dA_f \{u\} = -\{\delta u\}^T \rho \int_V [N]^T [N] dV \frac{\delta^2}{\delta t^2}\{u\} \\ +\{\delta u\}^T \int_{A_p} [N_n]\{P\} dA_p + \{\delta u\}^T \{F_e^{nd}\} \end{aligned} \tag{3.20}$$

and it can be reduced to

$$([K_e]+[K_e^f])\{u\}-\{F_e^{th}\}=[M_e]\{\ddot{u}\}+\{F_e^{pr}\}+\{F_e^{nd}\} \tag{3.21}$$

where $[K_e]$ is the element stiffness matrix, $[K_e^f]$ is the element foundation stiffness matrix, $\{F_e^{th}\}$ is the element thermal load vector, $[M_e]$ is the element mass matrix, $\{\ddot{u}\}$ is the acceleration vector (such as gravity effects) and $\{F_e^{pr}\}$ is the element pressure vector [SAS IP, 2007]. Simplified form of equation (3.21) that the finite element discretization process in Ansys yields is

$$[K]\{U\}=\{F^a\} \tag{3.22}$$

where $[K]$ is the system stiffness matrix, $\{F^a\}$ is the vector of applied loads and $\{U\}$ is the associated vector of nodal displacement [SAS IP, 2007].

## 3.2 Nonlinear Finite Element Formulation

For nonlinear analysis, the solution requires a linearization process where the nonlinear problem is transformed into a set of linear problems that follow the evolution of a configuration. Equilibrium positions are evaluated as the solution follows the equilibrium path in a step by step procedure, until the complete solution path has been obtained.

Various discretization schemes are possible while using the finite element method and the one used for nonlinear analysis in the finite element program ANSYS is the updated Lagrangian formulation [SAS IP, 2007]. In the updated Lagrangian formulation, all variables are referred to the current (i.e. from the end of the previous time step) configuration of the system while a formulation called total Lagrangian refers to the initial configuration as a frame of reference. In both formulations, equilibrium equations are obtained using the principle of virtual work and then linearized at the previously known configuration to yield incremental formulations for nonlinear analysis.

The assumption of infinitesimal deformation is not valid for nonlinear problems, so the initial and deformed configurations have to be distinguished. When a point $\mathbf{X}$ in the initial configuration moves to point $\mathbf{x}$ in the deformed configuration, the deformation gradient tensor $\mathbf{F}$ is given by

$$\mathbf{F}=\frac{\partial \mathbf{x}}{\partial \mathbf{X}} \tag{3.23}$$

The determinant of the deformation gradient **F** is defined as the Jacobian, $J = det\mathbf{F}$, and it gives the local volume change. Figure 3.1 illustrates the motion and position vectors of a deforming body.

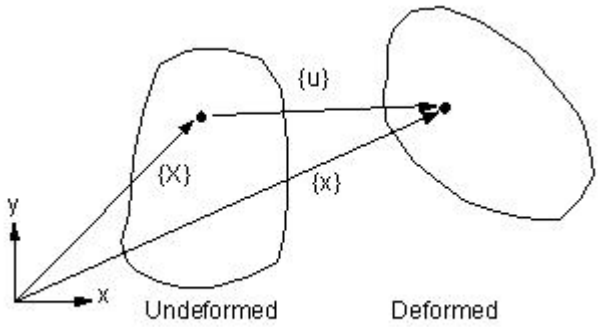


*Figure 3.1: Position vectors and motion of a deforming body [SAS IP, 2007].*

The updated Lagrangian formulation uses stress and strain measures defined at the current configuration, referred to as the Cauchy stress tensor $\sigma$ and the engineering strain tensor $\varepsilon$. The total Lagrangian formulation uses, however, the second Piola-Kirchhoff stress tensor **S** and the Green strain tensor $\varepsilon_{ij}^{el}$ defined at the initial configuration. The relation between the total Lagrangian and updated Lagrangian stress tensors can be obtained through the transformation as

$$\mathbf{S} = J\mathbf{F}^{-1}\sigma\mathbf{F}^{-\mathbf{T}} \tag{3.24}$$

The advantage of the updated Lagrangian formulation is the simplicity of incremental strain description but the disadvantage is that all derivatives with respect to spatial co-ordinates must be recomputed in each time step, because the reference configuration is changing [Miller et al., 2007].

The principle of virtual work is used, for both linear and nonlinear problems, to express the equilibrium of any deformed configuration. Capital letters are used here to design the variables in a reference configuration expressed as $C^i$ and small letters in the current configuration expressed as $C^t$. The volume in $C^t$ and $C^i$ is denoted by v and V, the part of the surface of $C^t$ and $C^i$ on which specified tractions $f_a$ and $F_a$ are applied is denoted by a and A and $f_v$ and $F_V$ are body forces in $C^t$ and $C^i$. The virtual work principle expressed in the

current configuration as reference is then given by

$$\{F_i^{nr}\} = \int_v \varepsilon_{ij}\sigma_{ij}dv - \int_v f_{vi}u_i dv - \int_a f_{ai}u_i da = 0 \tag{3.25}$$

and in the initial configuration,

$$\{F_i^{nr}\} = \int_v \varepsilon_{ij}S_{ij}dV - \int_V F_{Vi}U_i dV - \int_A F_{Ai}U_i dA = 0 \tag{3.26}$$

The vector $\{F_i^{nr}\}$ does not vanish if the current configuration is out of equilibrium and is then called the vector of residuals. In nonlinear analysis, the system stiffness matrix in equation (3.22) is itself a function of the unknown nodal displacements (or their derivatives) so the equilibrium equations can be written as

$$[K_i]^T\{\triangle U_i\} = \{F^a\} - \{F_i^{nr}\} \tag{3.27}$$

where $[K_i]^T$ is the Jacobian matrix, i is a subscript representing the current equilibrium iteration and

$$\{U_{i+1}\} = \{U_i\} + \{\triangle U_i\} \tag{3.28}$$

The values given by $\{U_i\}$ are used to evaluate both $[K_i]^T$ and $\{F_i^{nr}\}$. The right-hand side of (3.27) shows the amount the system is out of equilibrium.

The relationship between stress and strain can be nonlinear for structures with material nonlinearities. The stress is then a nonlinear function of the strain. The constitutive relations for a nonlinear elastic material which has no dependence on the history of the motion is given by,

$$\sigma = \kappa(\mathbf{F}) \tag{3.29}$$

where $\kappa$ is the material response function that depends only on the current value of the deformation gradient $\mathbf{F}$ and not on its history. A constitutive equation can not be expressed in terms of $\mathbf{F}$ unless the $\mathbf{F}$ dependence has a special form [Belytschoko et al., 2000].

## 3.3 Buckling Analysis

In a buckling analysis the buckling loads and the buckled mode shapes are determined. Buckling loads are critical loads where certain types of structures become unstable and buckled mode shape is the shape that the structure assumes in a corresponding buckled condition. For a long column subjected to compression axial forces, buckling occurs long before the normal stress reaches the strength of the column material. The failure can be described as failure due to elastic instability and it depends highly on the geometry and stiffness of the column. When the buckling loading is reached, the structure continues to deflect without an increase in the magnitude of loading. The buckling load and buckling mode shape of a structure can be determined with either linear eigenvalue or nonlinear buckling analysis. The eigenvalue buckling analysis predicts the Euler buckling load, or the theoretical buckling strength of an ideal linear elastic structure. The solution is usually approximate and overestimates the real buckling strength since it does not take into account the imperfections and nonlinearities that prevent most structures from achieving their theoretical elastic buckling strength. In a nonlinear buckling analysis the load is gradually increased until the structure becomes unstable and the model can include nonlinear features. While the eigenvalue technique gives no information about the post-buckled behavior of the structure, the nonlinear technique gives the complete behavior of the component before and after buckling [SAS IP, 2007].

### 3.3.1 Linear Eigenvalue Buckling Analysis

Linear eigenvalue buckling analysis predicts the theoretical buckling strength or the bifurcation point and it is assumed that there is no yielding of the material in the structure, the deflections are small and that the direction of applied forces does not change. The finite element discretization process in Ansys yields equation (3.22). For linear buckling the effect of the differential stiffness, the part of the stiffness matrix that is a function of the applied load, is added to the linear stiffness. In case of compressive loading it softens the total stiffness and in case of tensile loads it stiffens the total stiffness. When the structure buckles, the attribution of the differential stiffness causes the total stiffness matrix to become non positive. The buckling problems can be solved linear as eigenvalue problems, with the following buckling equation,

$$([K]+\lambda[K_d])\{U\}=0 \tag{3.30}$$

where $[K_d]$ is the differential stiffness matrix and $\lambda$ is the eigenvalue to be computed related to the buckling load. Once the eigenvalue is found, the critical buckling load is predicted as

the eigenvalue, λ, times the applied load,

$$\{F^{cri}\} = \lambda \cdot \{F^{a}\} \tag{3.31}$$

where $\{F^{cri}\}$ is the critical buckling load vector and $\{F^{a}\}$ is the applied load vector. There will be a number of buckling loads and mode shapes but the structure will fail when reaching the lowest critical buckling load so the higher-order buckling loads are usually not of interest. Therefore, only the lowest eigenvalue needs to be computed. Since this method does not take account of any initial imperfections and nonlinearities the results rarely agree with those determined in practice. Figure 3.2 shows how the real buckling strength is overestimated with linear buckling analysis.

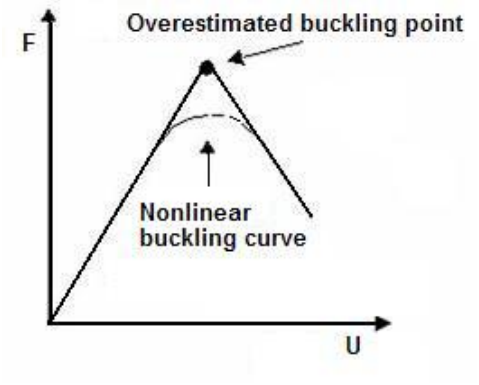


*Figure 3.2: Buckling point overestimated with linear eigenvalue analysis.*

In addition with overestimating the critical buckling load, the eigenvalue method of solution of buckling gives no information about the post-buckling behavior. Due to the shortcomings of linear eigenvalue analysis, nonlinear buckling analysis is often recommended for design or evaluation of actual structures.

### 3.3.2 Nonlinear Buckling Analysis

In nonlinear buckling analysis the loads are gradually increased to seek the load level at which the structure becomes unstable. This technique accounts for pre-buckled deformations and nonlinear features, such as material nonlinearity, geometric nonlinearity and initial imperfections. Common causes of nonlinear structural behavior are nonlinear stress-strain

relationships as well as the changing geometric configuration when a structure experiences large deformations. The load vectors and element matrices are derived using the updated Lagrangian formulation which produces equation (3.27) and the Newton-Raphson iterative method is used to solve the nonlinear variational equations. Figure 3.3 shows a single solution iteration of the Newton-Raphson method depicted graphically.

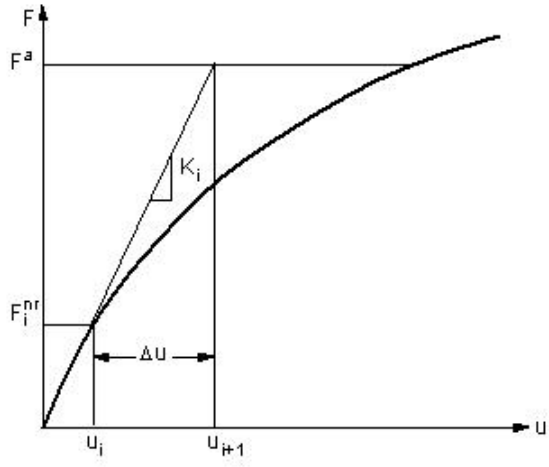


*Figure 3.3: Single solution iteration of the Newton-Raphson method [SAS IP, 2007]*

In order to obtain a converged solution, more than one Newton-Raphson iteration is needed. The subsequent iterations would proceed in a similar manner, as specified by the following general algorithm.

1. $\{U_0\}$ is assumed. $\{U_0\}$ is usually the converged solution from the previous time step but on the first time step $\{U_0\}$ is assumed to be $\{0\}$.
2. The updated tangent matrix $[K_i]^T$ and the restoring load $\{F_i^{nr}\}$ from configuration $\{U_i\}$ is computed.
3. Equation (3.27) is used to calculate $\{\triangle U_i\}$
4. Equation (3.28) is used to obtain the next approximation $\{U_{i+1}\}$
5. Steps 2 to 4 are repeated until convergence is obtained.

In Figure 3.4, the solution of two iterations is shown. The solution obtained at the end of the iteration process would correspond to load level $\{F^a\}$ that would be equal to the restoring load vector $\{F_i^{nr}\}$, such that the final converged solution would be in equilibrium.

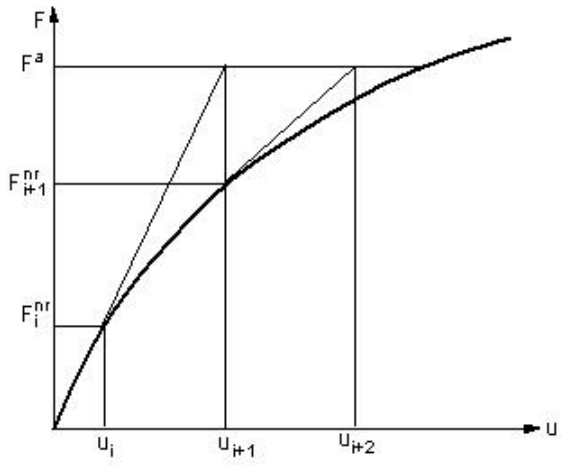


*Figure 3.4: Solution of two iterations of the Newton-Raphson method [SAS IP, 2007].*

If some path-dependent nonlinearities are included in the analysis, such as nonlinear stress-strain relationships, then some intermediate steps must be in equilibrium in order for the solution process to correctly follow the load path. This is accomplished by applying the load in increments and performing the Newton-Raphson iterations at each step,

$$[K_{n,i}]^T \{\triangle U_i\} = \{F_n^a\} - \{F_{n,i}^n\} \tag{3.32}$$

where $[K_{n,i}]^T$ is the Jacobian matrix for time step n, iteration i, $\{F_n^a\}$ is the total applied load vector at time step n and $\{F_{n,i}^{nr}\}$ is the restoring force vector for time step n, iteration i. Figure 3.5 shows this process known as the incremental Newton-Raphson procedure.

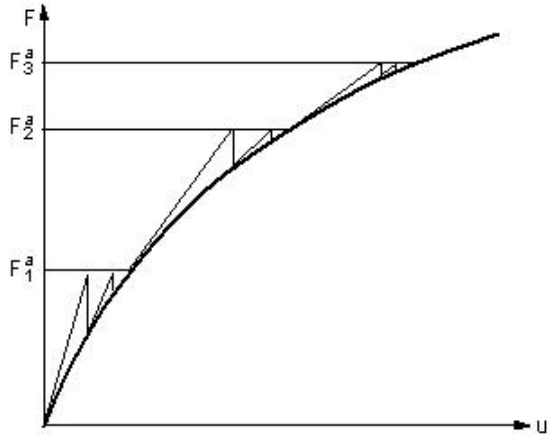


*Figure 3.5: The incremental Newton-Raphson procedure [SAS IP, 2007].*

Convergence is guaranteed with the Newton-Raphson method if and only if the solution at any iterations $\{U_i\}$ is near the exact solution.

# 4 Two Dimensional Finite Element Model

Structural analysis of a geothermal well using the finite element method provides very important input to the design process. The well's risk of failure depends not only on the materials compressive strengths, but also on the stress fields and the interactions between the cement and the steel in the well that can be simulated with a finite element model [Fleckenstein et al., 2005]. Here, a two dimensional axisymmetric finite element model of a geothermal well was developed, using the finite element program ANSYS. Three casings and a liner were modeled with axisymmetric shell elements and axisymmetric plane elements were used to model the formation and the cement around the casings. The connection behavior between the production casing and the cement is simulated with contact elements where the friction and maximum shear stress are defined. Figure 4.1 shows a part of the casings, the cement and the formation modeled in ANSYS.

First, a two dimensional thermal model was designed where the temperature distribution of the well can be examined, based on known temperature distribution inside the production casing and the temperature distribution for the ground where the temperatures of the well have no longer effect. Secondly, a two dimensional static structural model was made, where the temperature distribution resulting from the thermal analysis is used to examine the expansion of the production casing and the corresponding stresses. The models are parametrical, so different types of wells having different material properties, temperature distributions and pressure distribution inside the well can be examined. Different cases of connections between the steel in the production pipe and the cement around it can be explored as well, using the coefficient of friction and maximum shear stress parameters. The model is therefore useful when examining the rise of the production casing and to determine whether the stresses range over the materials yield stresses for different types of wells, in order obtain the proper design.

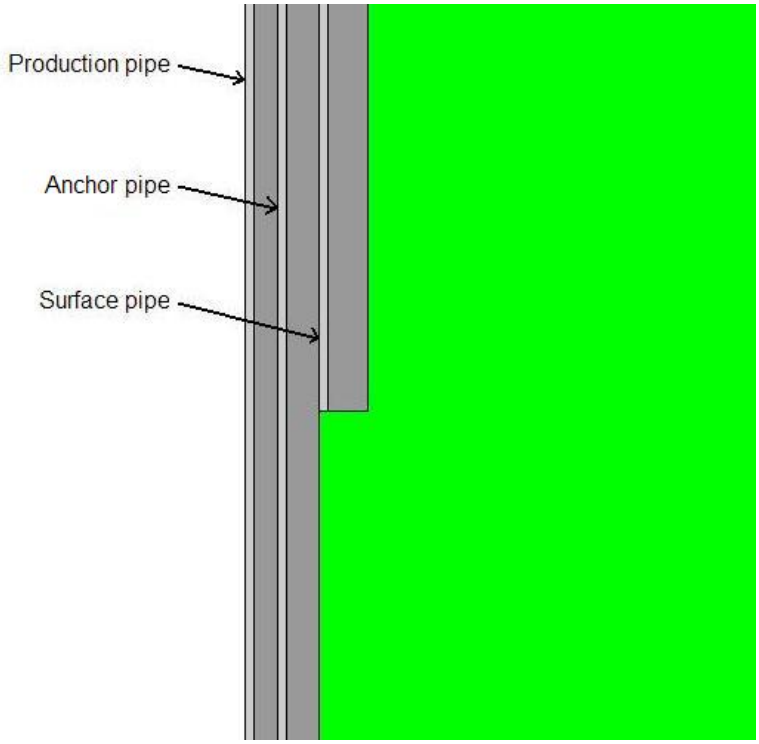


*Figure 4.1: Three casings (light grey), cement slurry around them (dark grey) and the surrounding formation (green) modeled using ANSYS (not to scale).*

## 4.1 Two Dimensional Thermal Model

The element type used in the two dimensional thermal model is plane77, a two dimensional eight node element. The element has one degree of freedom, temperature, at each node and axisymmetric behavior options as used in this model. Figure 4.2 shows the coordinate system, node locations and geometry for the element [SAS IP, 2007].

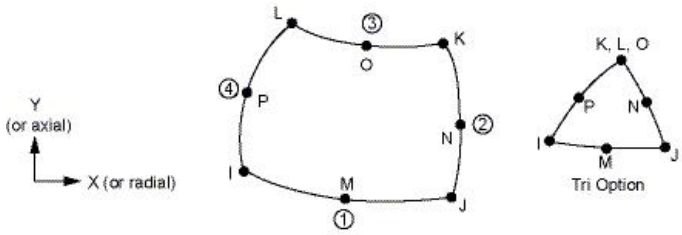


*Figure 4.2: The geometry, node locations and the coordinate system for element type plane77 [SAS IP, 2007].*

The material properties necessary for the thermal analysis of the well are the thermal conductivities of the steel, cement and the surrounding ground. The material directions are orthotropic corresponding to the element coordinate directions. The dimensional parameters needed for the two dimensional model are the outer radius, thickness and length of the surface pipe, security pipe, production pipe and the conductor as well as the radius of the ground that will be modeled surrounding the well.

Table 4.1 rounds up the dimensional parameters needed for the two dimensional model.

*Table 4.1:* Dimensional parameters

| Parameter | Description |
|---|---|
| Orsup: | Outer radius of surface casing [m] |
| Tsup: | Thickness of surface casing [m] |
| Lsup: | Length of surface casing [m] |
| Oranc: | Outer radius of anchor casing [m] |
| Tanc: | Thickness of anchor casing [m] |
| Lanc: | Length of anchor casing [m] |
| Orpp: | Outer radius of production casing [m] |
| Tpp: | Thickness of production casing [m] |
| Lpp: | Length of production casing [m] |
| Orlin: | Outer radius of the liner [m] |
| Tlin: | Thickness of the liner [m] |
| Llin: | Length of the liner [m] |
| Wground: | Radius of the ground [m] |

The dimensional parameters are graphically explained in Figure 4.3.

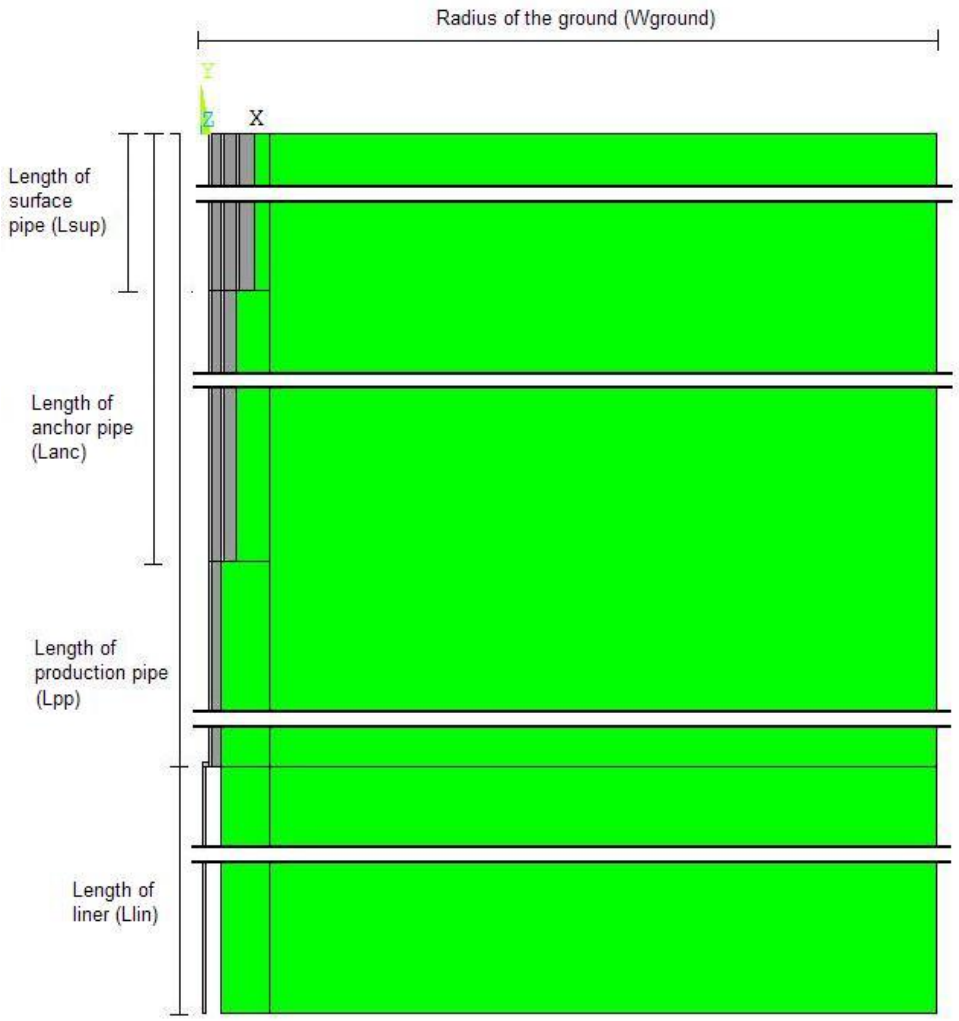


*Figure 4.3: Dimensional parameters of the two dimensional model.*

Table 4.2 shows the material properties needed for the two dimensional thermal model.

*Table 4.2:* Material properties for thermal analysis

| Parameter | Description |
|---|---|
| $K_{st}$: | Thermal conductivity for steel [$\mathrm{W}/(\mathrm{m}*^{\circ}\mathrm{C})$] |
| $K_{ce}$: | Thermal conductivity for cement [$\mathrm{W}/(\mathrm{m}*^{\circ}\mathrm{C})$] |
| $K_{gr}$: | Thermal conductivity for ground [$\mathrm{W}/(\mathrm{m}*^{\circ}\mathrm{C})$] |

In order to analyze the temperature distribution of the well, the temperature distribution inside the production casing is needed and the temperature distribution for the ground, where the temperature is no longer affected by the well's temperature. The distributions are expressed in a data file and the model's result is the temperature distribution of the entire well.

## 4.2 Two Dimensional Structural Model

The two dimensional structural model is not modeled in the same way as the thermal model because there are different features of interest that require a different setup of the model. The objective of the structural model is to estimate the stresses and the rise of the production casing, where plane elements, that are used in the thermal model, are not applicable. The availability of elements is very limited for coupled-field analysis, shell elements and the type of material model best suited for this structural model is not available. Coupled structural-thermal analysis in ANSYS is therefore not suitable for this model. Shell elements are instead used to model the casings in the structural analysis since they are better suited to simulate the thin columns in structural analysis than the plane elements.

The element type used for the steel, i.e. the casings and the liner, is shell209. It is an axisymmetric three node shell element with three degrees of freedom at each node, translations in the x and y directions and a rotation about the z-axis. The element is well suited for large strain nonlinear applications. Its geometry, node locations and element coordinate system is shown in Figure 4.4.

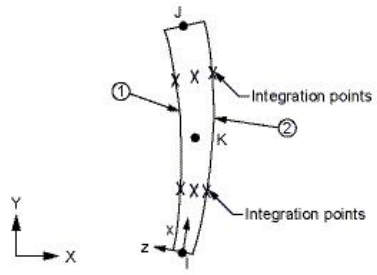


*Figure 4.4: The geometry, node locations and the coordinate system for element type shell209 [SAS IP, 2007].*

The element type plane183 is used to model the cement and the formation. Plane183 is defined by eight nodes and it has two degrees of freedom, translation in the nodal x and y directions, at each node. The element has axisymmetric capabilities as well as plasticity, large deflection and large strain capabilities. The geometry for the element is the same as for plane77, shown in Figure 4.2.

Contact elements are used to model the connection between the steel of the production pipe and the cement. The inner surface of the cement is defined as the target surface and the outer surface of the production pipe as the contact surface. The target and contact elements then make up a contact pair between the target and contact surfaces. The Coulomb friction model is used to control the contact behavior so the two contacting surfaces can carry shear stresses, $\tau$, up to a certain magnitude across their interface before they start sliding relative to each other. The shear stress is defined as a fraction of the contact pressure p,

$$\tau = \mu p + COHE \tag{4.1}$$

where $\mu$ is the coefficient of friction and COHE specifies the cohesion sliding resistance that provides sliding resistance even with zero normal pressure. The sliding will occur if the friction stress reaches the defined maximum contact friction stress, $\tau_{max}$, as demonstrated in Figure 4.5 [SAS IP, 2007].

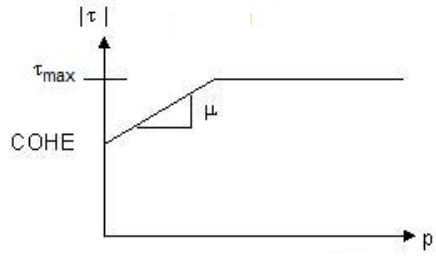


*Figure 4.5: Sliding contact resistance defined from cohesion, maximum contact friction stress and the coefficient of friction [SAS IP, 2007].*

The contact problems are highly nonlinear since they need to account for friction, making solution convergence difficult. The nonlinear formulation described in 3.2 is therefore the finite element formulation used in the models.

In this structural model, the two dimensional target segment targe169 is used to represent the target surface for the contact element conta172, which geometry is shown in Figure 4.6.

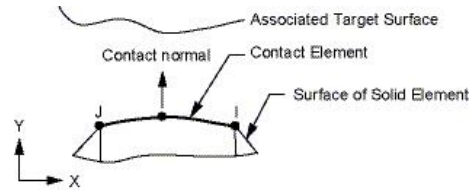


*Figure 4.6: The geometry of the contact element conta172 [SAS IP, 2007].*

The conta172 element has three nodes and the same geometric characteristics as the plane element face it is connected with. When the element surface penetrates one of the target segment elements, targe169, contact occurs.

The material properties defined for the structural model are the Young's modulus, poisson's ratio, density and the thermal expansion coefficient for the steel, cement and the ground. The nonlinear stress-strain curve is also defined for the steel and the cement. The temperature results from the thermal analysis are used as loads as well as the gravity and known pressure distribution inside the production pipe. Several degrees of freedom (d.o.f.) constrains can be used to analyze the thermal expansion of the well.

The additional material properties needed for the structural analysis are shown in Table 4.3.

*Table 4.3:* Material properties for structural analysis

| Parameter | Description |
|---|---|
| $E_{st}$: | Young's modulus for steel [Pa] |
| $P_{st}$: | Poisson's ratio for steel |
| $\rho_{st}$: | Density of steel [$Kg/m^3$] |
| $a_{st}$: | Thermal expansion coefficient for steel [$1/^\circ C$] |
| $\mu_{st}$: | Coefficient of friction between steel and concrete |
| $E_{ce}$: | Young's modulus for cement [Pa] |
| $P_{ce}$: | Poisson's ratio for cement |
| $\rho_{ce}$: | Density of cement [$Kg/m^3$] |
| $a_{ce}$: | Thermal expansion coefficient for cement [$1/^\circ C$] |
| $E_{gr}$: | Young's modulus for the ground [Pa] |
| $P_{gr}$: | Poisson's ratio for the ground |
| $\rho_{gr}$: | Density of the ground [$Kg/m^3$] |
| $a_{gr}$: | Thermal expansion coefficient for the ground [$1/^\circ C$] |

The d.o.f. constraints are specified in the model as well as the stress-strain curve for the steel and the cement. The pressure distribution inside the production pipe is expressed in a data file, like the temperature distribution.

It is assumed that the well's temperature is the same as the ground's temperature before the well is brought into production. The thermal strains in the well are therefore due to the temperature difference between the ground's temperature distribution and the temperature distribution of the well, resulting from the thermal model. The temperature difference is transferred from the thermal model and used as body force loads in the structural model. The results from the structural analysis are the expansions of the well due to the loads and the corresponding stresses, that can be taken into consideration when designing the well.

# 5 Three Dimensional Finite Element Model

A three dimensional model was made in ANSYS to examine the buckling behavior of a geothermal well's innermost casing. The results from the two dimensional thermal analysis are used as loading in the 3d analysis. Furthermore, gravity and known pressure distribution inside the production pipe is taken into account. As for the two dimensional analysis, three casings, cement around the casings, a conductor and the surrounding formation were modeled. The radius of the ground was, however, modeled smaller and the model was modeled with 3d finite elements only down to a specific depth due to size limitations of the ANSYS student version. The rest is kept with 2d finite elements that are transferred from the 2d structural model to the 3d model in order to reduce the computer solving time. The displacement constraints from the 2d structural analysis are used on the outer surface of the ground and on the bottom of the well if the entire well is not modeled, in order to simulate the real behavior of the well. It is only necessary to model one half of the well, where the well is divided about a plane parallel to the length of the well as shown in Figure 5.1, because the buckling failure mode considered is symmetric about that plane.

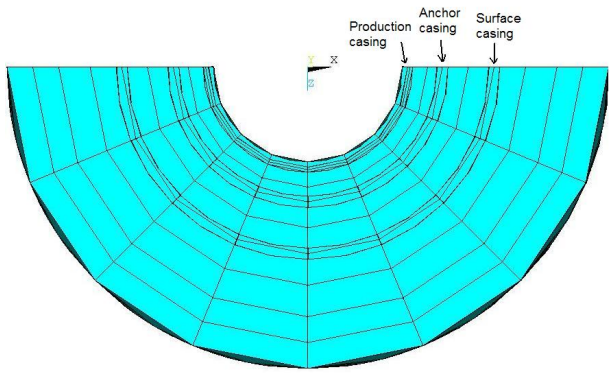


*Figure 5.1: The top view of the well modeled using ANSYS.*

The casings are modeled with shell elements and the cement slurry with solid elements. Due to the enormous size of the three dimensional model, the computer solving time is excessive, and the node number is too high for the student version of ANSYS. The model was therefore reduced by having only a small part of the well, where the buckling is estimated to occur, with contact elements between the production casing and the surrounding cement. The rest of the elements at that connection are merged together, so the buckling of the production pipe will occur at the location having contact elements. Figure 5.2, shows the cross section of the small part modeled with contact elements.

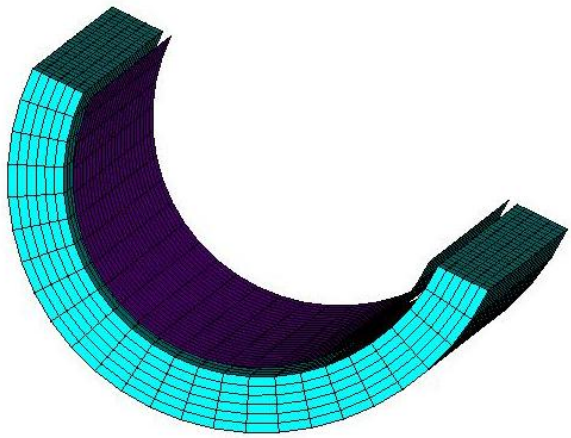

*Figure 5.2: The cross section of the part modeled with contact elements.*

However, if the computer resources used are powerful enough, contact elements can be defined everywhere between the casing and the cement and a larger part of the well can be modeled. Figure 5.3 shows a segment of the well, where the part in the middle having smaller elements is the part with contact elements.

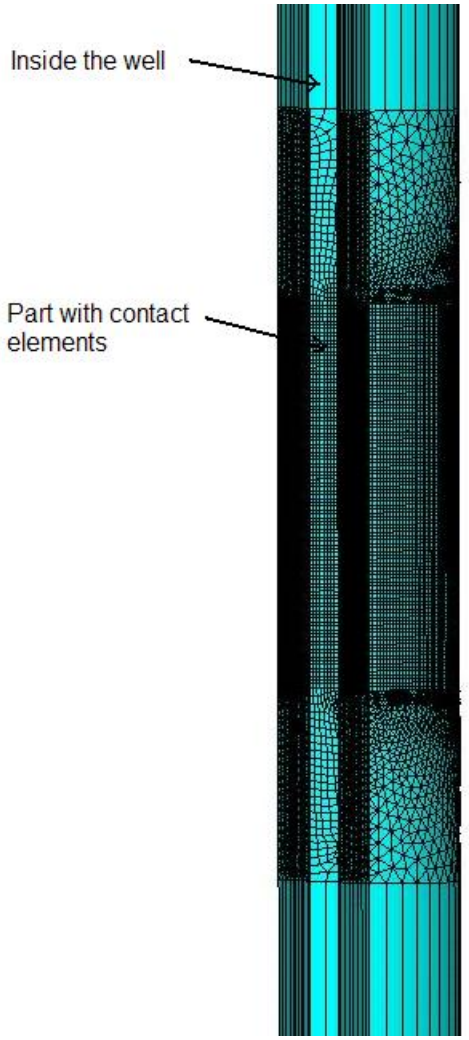


*Figure 5.3: A part of the well modeled using ANSYS.*

## 5.1 Three Dimensional Buckling Model

The element type used for the shell elements in the three dimensional model is shell93, a eight node structural shell well suited to model curved shells. The element has six degrees of freedom, translations in the nodal z, y, and z directions and rotations about the nodal z, y, and z axes, at each node. Figure 5.4 shows the geometry, node locations, and the coordinate system for the element, which has plasticity, large deflection and large strain capabilities.

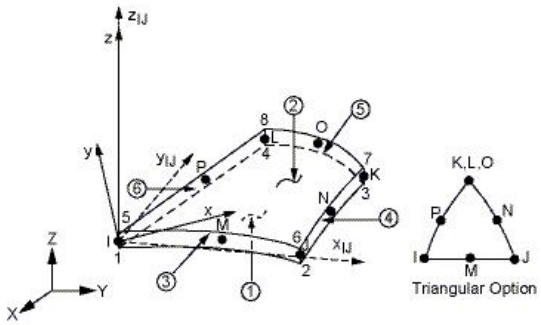


*Figure 5.4: The geometry, node locations and the coordinate system for element type shell93 [SAS IP, 2007].*

Solid95, a three dimensional 20 node structural solid element, was used to model the ground and the cement around the casings. Figure 5.5 shows the geometry, node locations, and the coordinate system for the element.

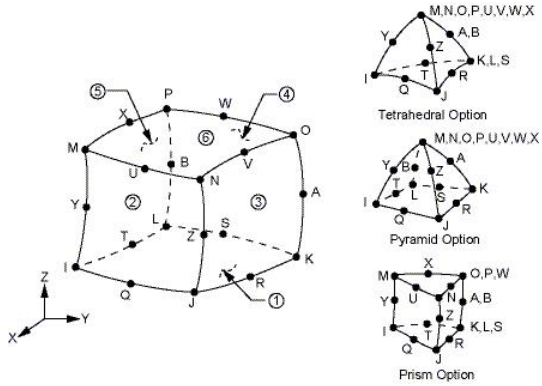


*Figure 5.5: The geometry, node locations and the coordinate system for element type solid95 [SAS IP, 2007].*

Solid95 has three degrees of freedom at each node, translations in the nodal x, y, and z directions, and it is well suited to model curved boundaries. The element has also plasticity, large deflection and large strain capabilities like shell93.

The contact element type used in the 3d model is conta174 and the target element type is targe170. The geometry of the elements can be seen in Figure 5.6.

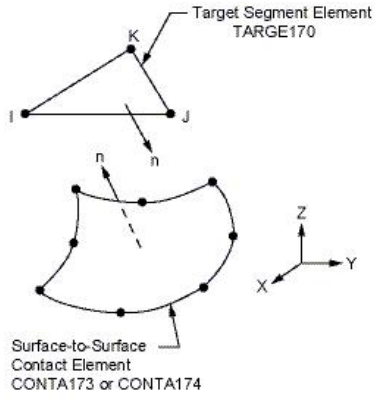


*Figure 5.6: The geometry, node locations and the coordinate system for element types conta174 and targe170 [SAS IP, 2007].*

The same dimensional parameters and material properties are used as for the two dimensional structural analysis. The temperature difference between the ground's temperature distribution and the temperature distribution of the well resulting from the two dimensional thermal model are used as loads, as well as the pressure distribution inside the production pipe and gravity. The nodes are coordinated between the two models, in order to put the right temperature difference on the nodes in the three dimensional model. D.o.f. displacement constraints are also defined at the nodes on the outer surface of the ground and as mentioned before at the bottom of the well if the entire length is not modeled, based on the results from the two dimensional structural analysis. Figure 5.7 shows how the models are linked together.

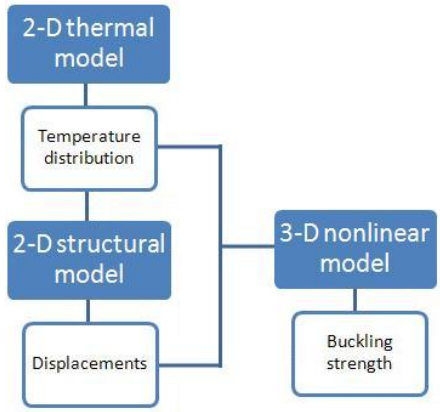


*Figure 5.7: Information used in the three dimensional model from the two dimensional models.*

The temperature distribution resulting from the thermal model is used in the 2d structural model and in the 3d nonlinear model. The displacements from the 2d model are also used in the 3d model. Table 5.1 explains the two dimensional parameters needed additionally for the 3d analysis, along with the parameters used in the 2d models.

*Table 5.1:* Additional dimensional parameters needed for the three dimensional model

| Parameter | Description |
|---|---|
| zpart: | Z-location (positive) where the part with contact element starts [m] |
| lpart: | Length of the part with contact elements [m] |

Element sizes needed for the three dimensional model are graphically explained in Figure 5.8.

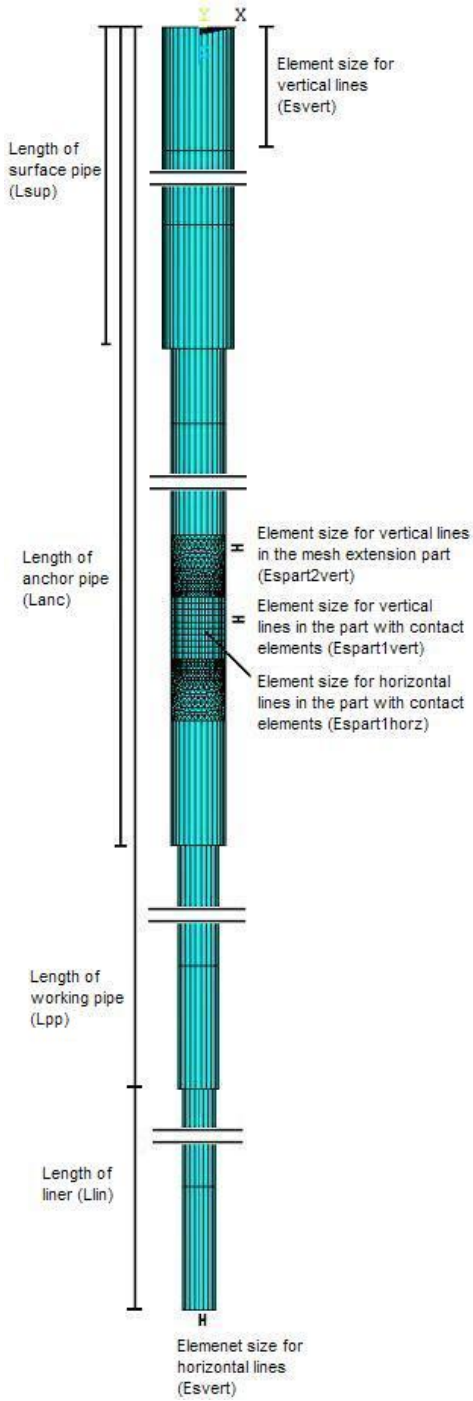


*Figure 5.8: Parameters for lengths and element sizes in the three dimensional model.*

If the model is used to perform a structural analysis, the results are the thermal expansion of the well and the stress magnitudes, due to the assumed loads. The nonlinear buckling analysis results are the buckling mode shape and the buckling strength. In that case, a sideward pressure is used to obtain instability in the well. The inward pressure acting on the production pipe could result from fluid trapped in the cement outside the casing or due to the flash zone inside the well. The liquid flashes into vapor in the flash zone with corresponding pressure and temperature changes. The pressure is modeled where the contact elements are located, where the buckling failure is enabled.

# 6 Case Study

## 6.1 Well Configurational Data

A case study is performed in order to examine how the model functions and how it responds to the properties of a geothermal well. The case study shows thermal and structural two dimensional analyzes as well as three dimensional buckling analysis of a 2300 m deep geothermal well. It is endeavored to have the parameters defined in the model as close as possible to a typical geothermal well, but some assumptions are made. The main objective is to study how the model reacts to the prerequisites assumed. The production casing in the model is 9 5/8 inches and all of the casings are assumed to be made of K55 carbon steel.

Typical material properties are used for the steel and the friction coefficient between the steel and the cement is assumed to be $\mu = 0.5$, as shown in Table 6.4 [Li and Mobashert, 1998].

*Table 6.1:* Material properties for the steel used in the case study.

| Description | Param. | Value |
|---|---|---|
| Young's modulus for steel | $E_{st}$: | $210 \cdot 10^9$ Pa |
| Poisson's ratio for steel | $P_{st}$: | 0.3 |
| Density of steel | $\rho_{st}$: | 7850 $\mathrm{Kg/m^3}$ |
| Thermal conductivity for steel | $K_{st}$: | 46 $\mathrm{W/(m*^\circ C)}$ |
| Thermal expansion coefficient for steel | $a_{st}$: | $12{\cdot}10^{-6}$ $1/^\circ$C |

The parameters used for the material properties of the cement are shown in Table 6.5 [Gretarsdottir, 2007].

*Table 6.2:* Material properties for the cement used in the case study.

| Description | Param. | Value |
|---|---|---|
| Young's modulus for cement | $E_{ce}$: | $2.98 \cdot 10^9$ Pa [Gretarsdottir, 2007] |
| Poisson's ratio for cement | $P_{ce}$: | 0.15 [Gretarsdottir, 2007] |
| Density of cement | $\rho_{ce}$: | 1666 $Kg/m^3$ [Gretarsdottir, 2007] |
| Thermal conductivity for cement | $K_{ce}$: | 0.81 $W/(m \cdot ^\circ C)$ [Gretarsdottir, 2007] |
| Thermal expansion coefficient for cement | $a_{ce}$: | $9.07 \cdot 10^{-6}$ $1/^\circ C$ [Gretarsdottir, 2007] |
| Coefficient of friction between steel and cement | $\mu_{st}$: | 0.5 [Li and Mobashert, 1998] |

Table 6.3 shows the material properties assumed for the surrounding formation.

*Table 6.3:* Material properties for the formation used in the case study.

| Description | Param. | Value |
|---|---|---|
| Young's modulus for the ground | $E_{gr}$: | $100 \cdot 10^9$ Pa [H., 2009] |
| Poisson´s ratio for the ground | $P_{gr}$: | 0.31 [Christensen, 1995] |
| Density of the ground | $\rho_{gr}$: | 2650 $Kg/m^3$ [Björnsson and Hjartarson, 2003] |
| Thermal conductivity for ground | $K_{gr}$: | 2 $W/(m * ^\circ C)$ [Axelsson, 2009] |
| Thermal expansion coefficient for the ground | $a_{gr}$: | $5.4 \cdot 10^{-6}$ $1/^\circ C$ [Encyclopædia Britannica, 2009] |

The dimensional parameters used in the model are rounded up in Table 6.4 and the casings' sizes are illustrated in Figure 6.1 [Karlsdottir, 2008]. The parameters are typical dimensional parameters for a high temperature geothermal well and the radius of the formation modeled is 200 m, so that it properly simulates the stiffness and forces due to the ground surrounding the well.

*Table 6.4:* Dimensional parameters used in the case study [Karlsdottir, 2008].

| Description | Parameter | Size |
|---|---|---|
| Outer radius of surface casing | Orsup: | 0.2301875 m |
| Thickness of surface casing | Tsup: | 0.013 m |
| Length of surface casing | Lsup: | 30 m |
| Outer radius of anchor casing | Oranc: | 0.1698625 m |
| Thickness of anchor casing | Tanc: | 0.013 m |
| Length of anchor casing | Lanc: | 150 m |
| Outer radius of production casing | Orpp: | 0.1222375 m |
| Length of production casing | Tpp: | 0.012 m |
| Length of production casing | Lpp: | 800 m |
| Outer radius of the liner | Orlin: | 0.0968375 m |
| Thickness of the liner | Tlin: | 0.012 m |
| Length of the liner | Llin: | 1500 m |
| Radius of the ground | Wground: | 200 m |

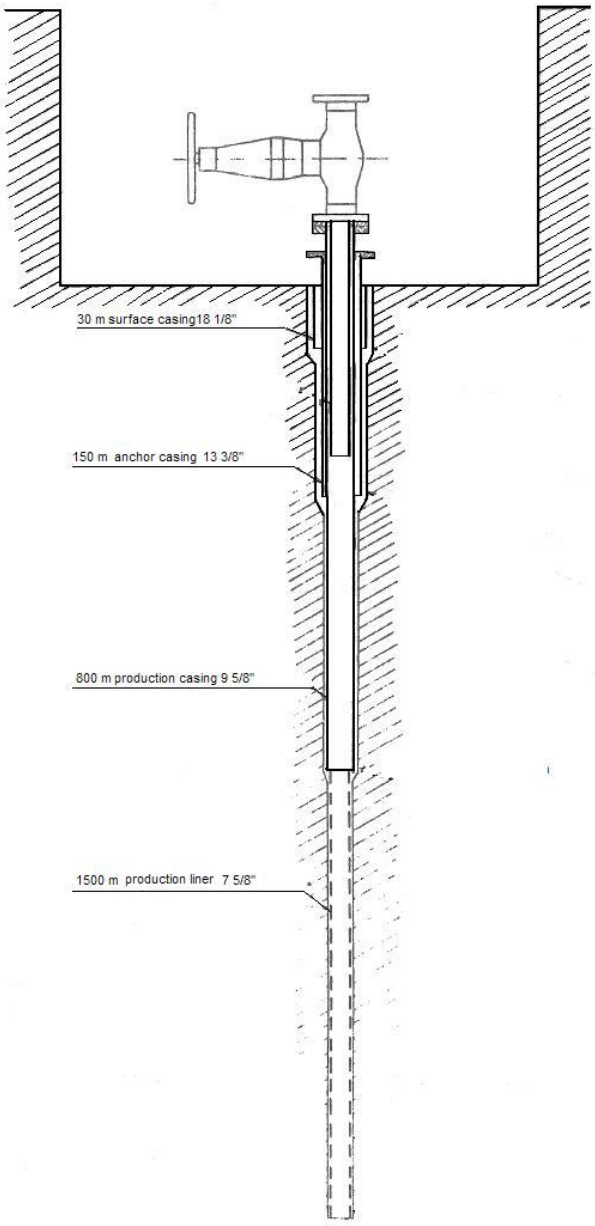


*Figure 6.1: The well studied with the finite element model in this project.*

The stress-strain curve for the steel at room temperature is shown in Figure 6.2 [Karlsdottir, 2008].

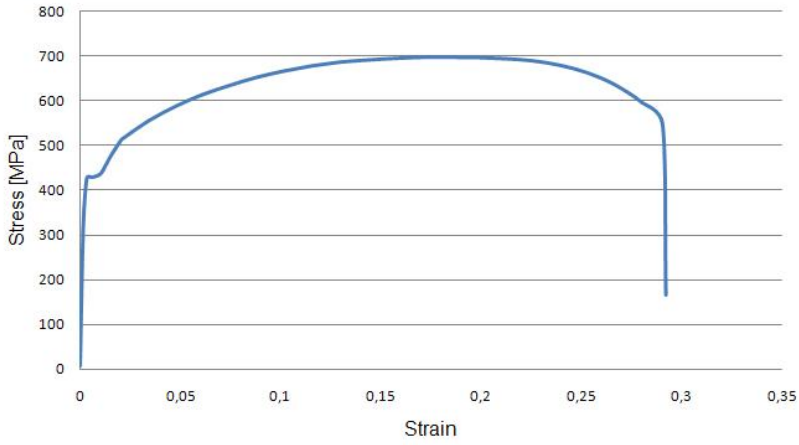


*Figure 6.2: Stress-strain curve for steel K55.*

Plastic deformation of the steel will occur if the stress exceeds the yield stress of the steel, which is around 425 MPa in this case. The stress-strain curve for the cement at room temperature is illustrated in Figure 6.3 [Gretarsdottir, 2007].

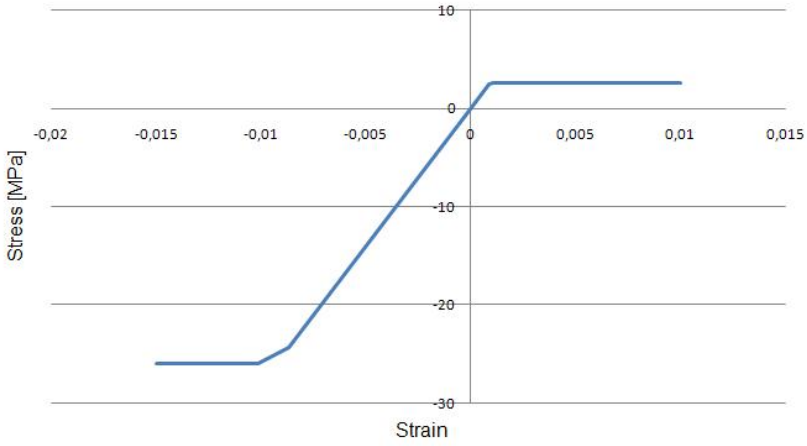


*Figure 6.3: Stress-strain curve used for the cement.*

The yield stress is different in compression and in tension for the cement. It is around 26 MPa in compression but ten times lower in tension, or 2.6 MPa. The pressure and temperature distribution inside the well and the temperature distribution of the ground used in the case study, is shown in Table 6.5. Those distributions were measured for well NJ-18 at Nesjavellir [Sigurðsson and Gunnlaugsson, 1989].

*Table 6.5:* Pressure and temperature distributions used in the case study.

| Depth [m] | Temperature inside the well [$^{\circ}C$] | Pressure inside the well [Pa] | Temperature of the formation [$^{\circ}C$] |
|---|---|---|---|
| 0 | 155.0 | 450000 | 3.0 |
| 100 | 158.0 | 519000 | 6.0 |
| 200 | 160.0 | 645000 | 14.0 |
| 302 | 162.4 | 813000 | 25.0 |
| 400 | 173.0 | 1008000 | 41.0 |
| 504 | 184.0 | 1283000 | 52.0 |
| 603 | 194.5 | 1656000 | 74.0 |
| 700 | 197.0 | 2421000 | 109.0 |
| 800 | 200.0 | 3273000 | 162.0 |
| 900 | 202.3 | 4145000 | 179.0 |
| 1000 | 202.7 | 5011000 | 186.0 |
| 1100 | 203.4 | 5865000 | 193.0 |
| 1200 | 204.0 | 6719000 | 199.0 |
| 1402 | 206.0 | 8449000 | 204.0 |
| 1607 | 219.0 | 10195000 | 204.2 |
| 1700 | 237.4 | 10976000 | 206.0 |
| 1800 | 250.9 | 11782000 | 219.0 |
| 1900 | 262.2 | 12200000 | 237.4 |
| 1984 | 262.2 | 13242000 | 250.9 |

The maximum shear stress parameter used in the model to define the contact behavior was estimated by performing a push-out test, which is an experimental technique widely used to evaluate shear stiffness and shear strength. The experiment was performed in cooperation with ICI Rheocenter at the Innovation Center Iceland. The result of the interfacial shear strength for an unmodified cement slurry after 28 days, is 0.72 MPa so the $\tau_{max}$ parameter in the model is set as 0.72 MPa. The experiment was not performed under the same temperature conditions as in an actual geothermal well, which might affect the results. The additionally pressure on the cement, due to its weight, is also not simulated in the experiment, but it might cause more connection to the steel. More information about the experiment can be seen in Appendix A.

## 6.2 Two Dimensional Thermal Analysis

The two dimensional thermal analysis gives the steady state temperature distribution of the well, based on the parameters defined in the above section. The temperature of the formation, casings and cement rises along the production pipe due to thermal conduction from the water temperature inside the well. The heat is conducted through the casings and the cement to the formation as can be seen in Figure 6.4.

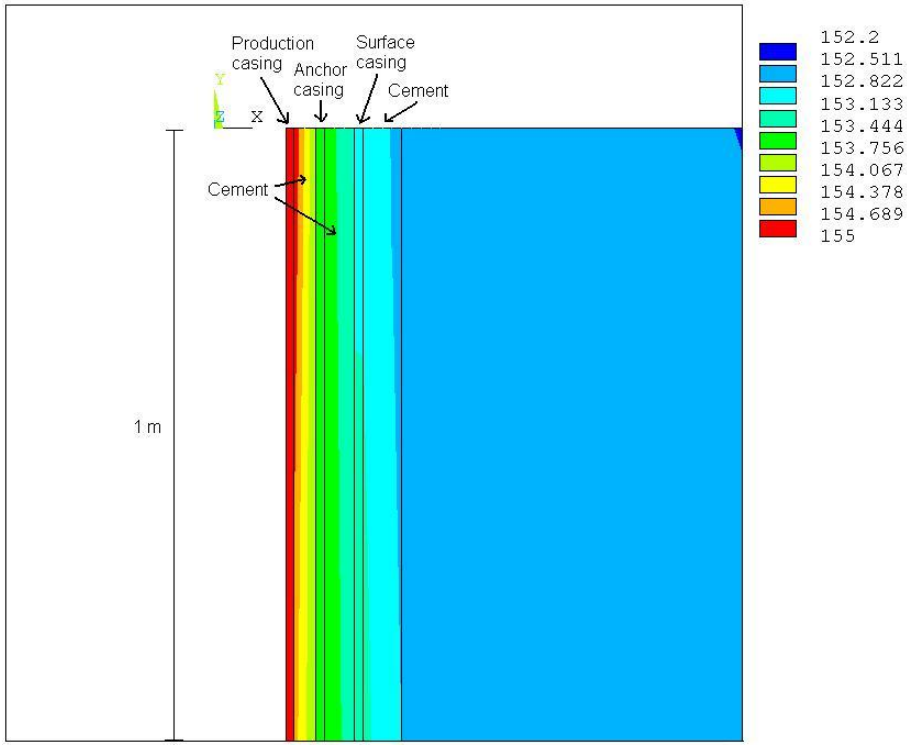


*Figure 6.4: Temperature conduction through the casings and cement to the formation at the top 1 m of the well* [$^{\circ}C$].

The temperature difference between the inner side of the production casing and the outer side of the cement around the surface casing, is only 2-3 $^{\circ}C$ as shown in the figure above. The conduction is higher through the steel then through the cement, because the thermal conductivity is higher for steel.

## 6.3 Two Dimensional Structural Analysis

The objective of the structural analysis is to estimate the maximum rise of the production casing and to examine the stress distribution of the well. The equations used to calculate the thermal strains and stresses are explained in section 3.1. The well defined in section 6.1 was modeled, but with linear material properties.

Figure 6.5 shows a part of the temperature difference that is used as body force loads in the structural model. The load transfer from the thermal model is explained in section 4.2.

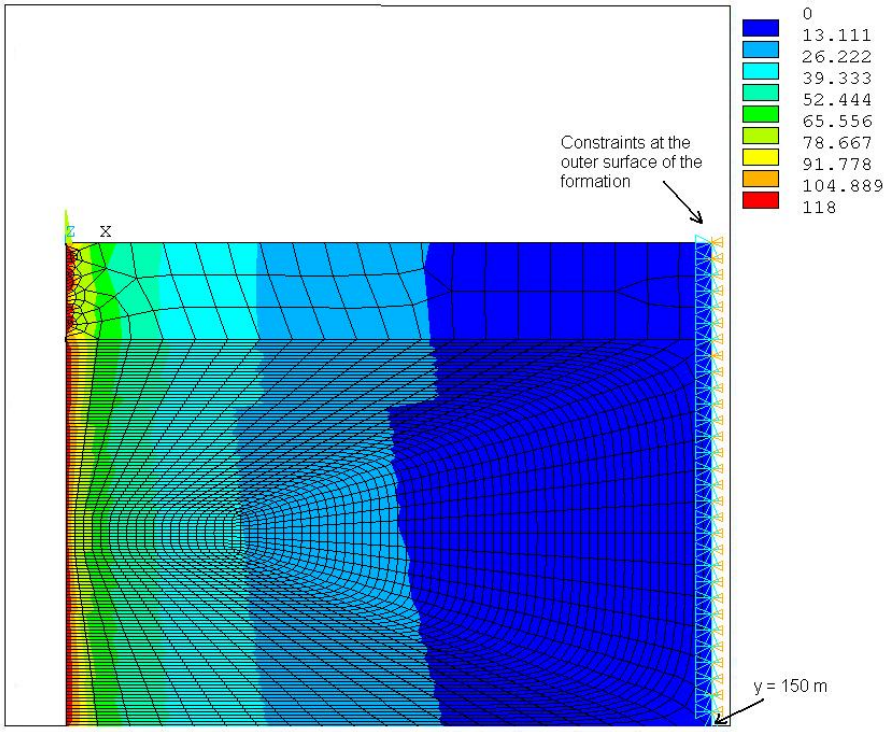


*Figure 6.5: Temperature difference used as body force loads [°C].*

The temperature difference shown is from the surface of the well down to 150 m, and the contour has been redefined to make the load distribution more detectable. The maximum difference is 152 °C at the surface of the cement beside the production casing. The temperature of the cement at that location is 155°C after the well is brought to production (see Figure 6.4), but the same as the formation temperature before it is brought to production, 3°C.

### 6.3.1 Displacements

The maximum displacements of the production casing were examined for five different cases. Some part of the production pipe must be merged with the cement, in order for the model to converge, i.e. the contact behavior can not be defined with the contact elements for the entire pipe. The part merged together must also be large enough to prevent the forming of high pressure tops around the fixed part, so three cases were defined with various parts merged together.

In case 1, a 400 m long part between the end of the anchor pipe, at 150 m, and down to 550 m is merged together. Contact elements are used above the end of the anchor pipe and below the merged part to simulate the connection between the steel in the production pipe and the cement. The other casings and the cement around them are also merged together as well as the cement and the ground, but the liner is only fixed to the production pipe at the top. The formation is constrained so the entire outer surface is fixed as well as the bottom of the formation. The greatest upward displacements for case 1 are at the top of the well, shown in Figure 6.6.

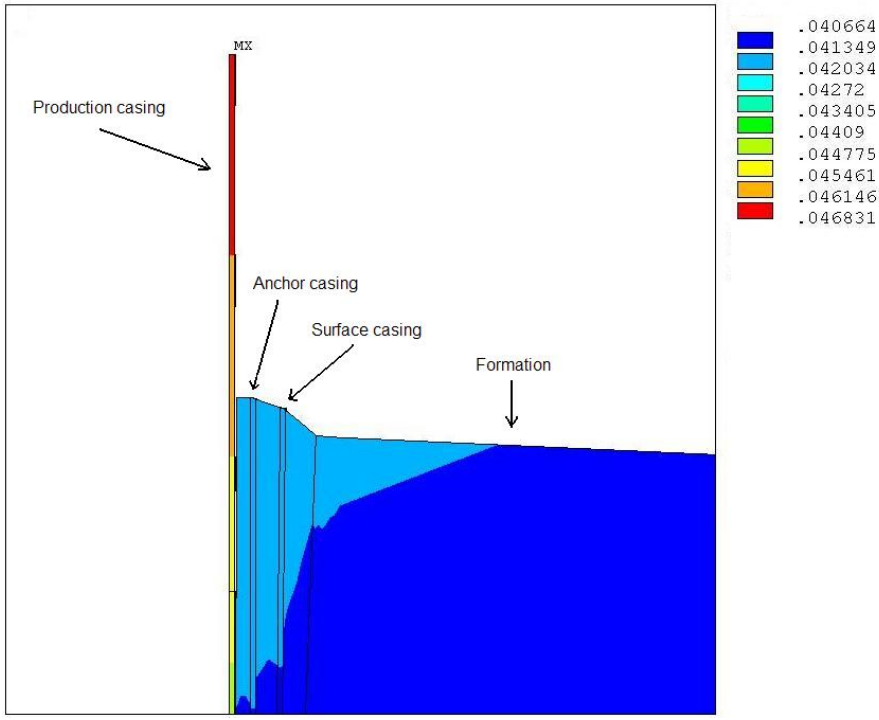


*Figure 6.6: The y-displacement at the top of the well for case 1 [m].*

The y-displacement increases along the production casing to the top, where the maximum upward displacement is 0.0468 m while the maximum downward displacement is 0.6576 m at the bottom of the production liner. The large downward displacement of the liner occurs because the liner can move without restraint down, since it is not connected to the formation. An upward rise of around 0.13 m has been detected in the casings at the power plant Hellisheidi in Iceland which is considerably higher than the model's results [Gretarsdottir, 2007]. There are some uncertainty factors in the model that could affect the results. The constraints on the model can for example greatly affect the results, so they must be chosen carefully.

In case 2, contact elements were defined except from the depth of 400 m to 600 m, instead of 150 m to 550 m in case 1, in order to examine its effect. This specific part is chosen to be fixed because sliding can then occur on a larger part between the steel and the cement since the fixed part has been halved. Additionally a larger part of the casing can expand upwards since the fixed part is located deeper in the well. The difference in results for the maximum upward displacement in case 1 and case 2 is though only of the order of $10^{-4}$ so the effect of decreasing the fixed part and locating it deeper in the well is negligible. The friction stress between the steel and the cement is almost everywhere below the maximum friction stress defined as 0.72 MPa in the model, but it reaches 0.72 MPa on a small part at the top of the casing, where sliding occurs. Figure 6.7 shows the friction stress between the cement and the production casing at the top of the well for case 2.

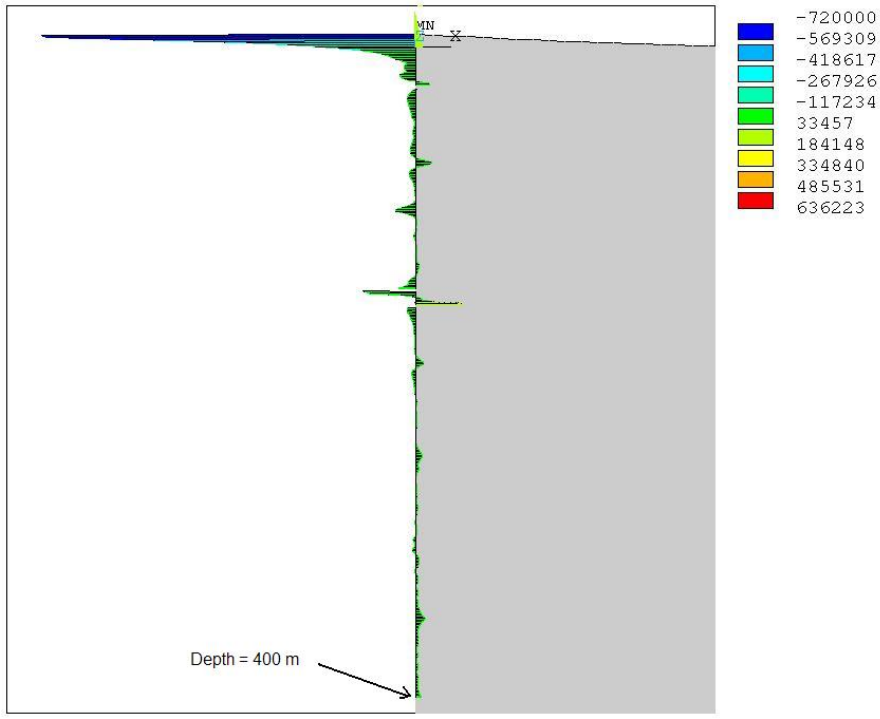


*Figure 6.7: The friction stress between the steel and the cement at the top of the well for case 2 [Pa].*

The small difference in results when the fixed part is decreased and lowered, is probably because the friction stress is mostly not reaching the maximum friction stress defined, so sliding occurs only on a small part at the top. The contact behavior is therefore likely to be similar to a case where the production casing is completely fixed to the cement.

In order to estimate whether it affects the results to decrease the fixed part even more and locate it deeper in the well, case 3 was studied. In case 3, the fixed part is ranging from 700 m to 800 m. The production casing is 800 m long, so the fixed part is located at the bottom of the pipe. The results were the same as for case 2, so it does not affect the results to decrease the fixed part and locate it deeper than in case 2.

Table 6.6 rounds up the results for the maximum upward rise of the production casing, for the three cases mentioned above.

*Table 6.6:* Comparison of the y-displacements of the production pipe based on the connection between the production casing and the cement.

| Connection between steel and cement | Maximum upward displacement at the top [m] |
|---|---|
| Case 1: Fixed from 150 m to 550 m: | 0.0468 |
| Case 2: Fixed from 400 m to 600 m: | 0.0470 |
| Case 3: Fixed from 700 m to 800 m: | 0.0470 |

The size of the fixed part between the production casing and the cement around it does not seem to affect the results of the maximum upward displacement of the production casing. The contact behavior defined by the contact elements might therefore be similar to the behavior when the connection is fixed together.

In case 4, the friction coefficient and the maximum friction stress are set so high that no sliding can occur between the steel and the cement in order to examine whether the difference is small between that case and the cases where the contact behavior is as defined as in section 6.1. The completely fixed part is the same as for case 1, i.e. from 150 m to 550 m. The maximum rise for case 4 is 0.0434 m as shown in Figure 6.8, with the same contours as in Figure 6.6 to enable comparison between the two cases.

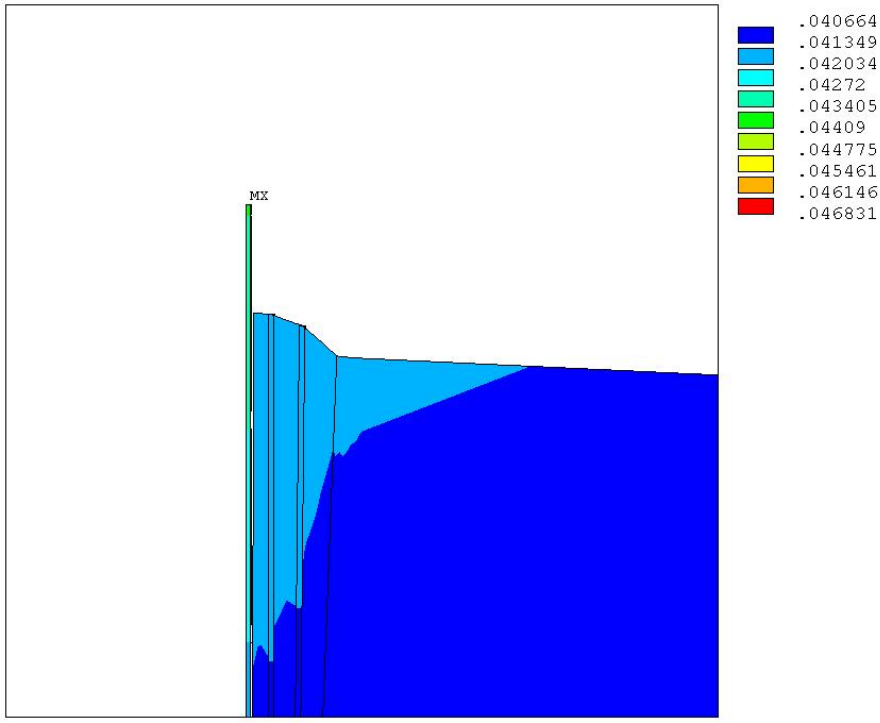


*Figure 6.8: The y-displacement at the top of the well when no sliding can occur between the steel and the cement [m].*

The comparison of figures 6.8 and 6.6 reveals the difference in upward expansion at the top of the well, between the case with contact elements as defined in section 6.1, and the case where the contact properties are defined so no sliding can occur between the steel and the cement. The difference of the maximum displacement of the production casing is only around 0.0034 m, so the contact elements, as defined in section 6.1, only permit sliding on a small part of the casing.

The result is much higher though for the maximum rise of the production casing when no contact elements are defined, as in case 5. The maximum displacement of the production casing is 0.2702 m in that case. Then there is no friction or maximum shear stress between the casing and the cement on that part and the production casing can move freely except from the fixed part which is the same as for case 1 and 4, i.e. between 150 m and 550 m. Table 6.7 shows the comparison between cases 4 and 5.

*Table 6.7:* Comparison of the y-displacements of the production pipe for no contact and a fixed case.

| Connection between steel and cement | Maximum upward displacement at the top [m] |
|---|---|
| Case 4: High friction, and fixed from 150 m to 550 m: | 0.0434 |
| Case 5: No contact but fixed from 150 m to 550 m: | 0.2702 |

The connection between the steel and the cement greatly affects the displacement results of the production pipe. The displacements are much lower when the contact elements simulate the friction and maximum shear stress between the steel and the cement, as in cases 1-4, than if there is no contact as in case 5. They are, however, close to the results when the friction coefficient of the contact elements is high. The explanation might be that the friction stress does not reach the maximum friction stress defined in the model, except for a small part. It is therefore important to discover whether the cement breaks away from the steel or whether it behaves according to the experimental values of the coefficient of friction and maximum shear stress, in order to use the model to estimate the rising of geothermal casings.

### 6.3.2 Stress magnitudes

The von Mises stress distribution at the top of the well, for case 1, when the casing is estimated to be fixed from 150 m to 550 m, is shown in Figure 6.9.

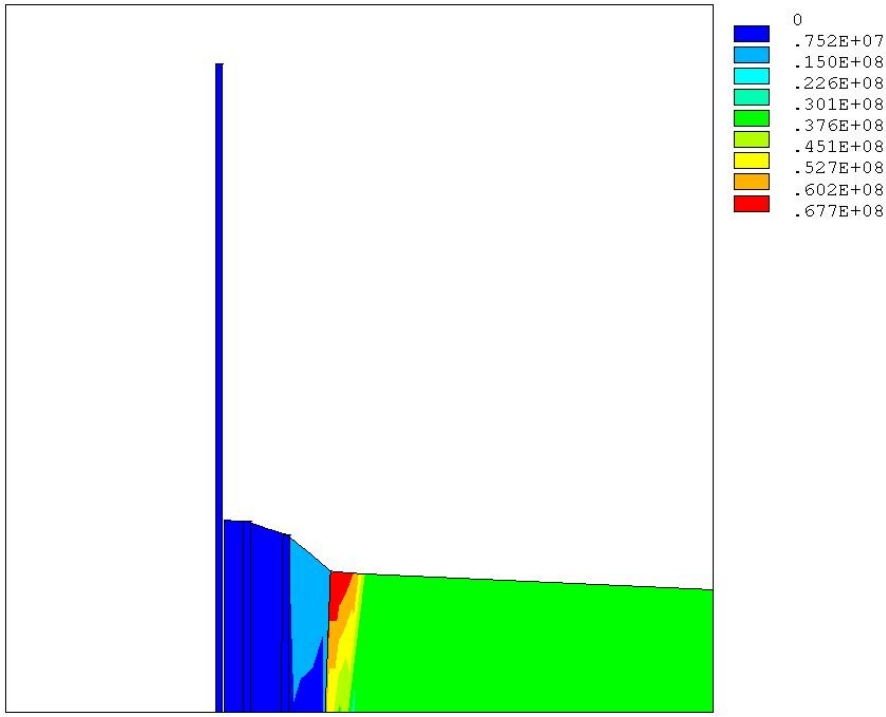


*Figure 6.9: The von Mises stress distribution at the top of the well for case 1 [Pa].*

The highest von Mises stresses are located in the formation next to the cement around the surface pipe. The stress magnitude is lower closer to the surface pipe as the figure illustrates.

The maximum von Mises stress of the pipes is 334 MPa at the fixed part of the production pipe, so plastic deformation does not occur according to the the yield stress of the steel defined as 425 MPa. The experiments used to define the yield stress were performed at room temperature so the real yield stress is probably closer to 380 MPa as defined in [Wu et al., 2005]. Anyhow, the maximum stress results of the steel in the model does not reach the yield stress of the steel.

The y-components of the stresses are examined for the cement. The stresses for the top of the well can be seen in Figure 6.10.

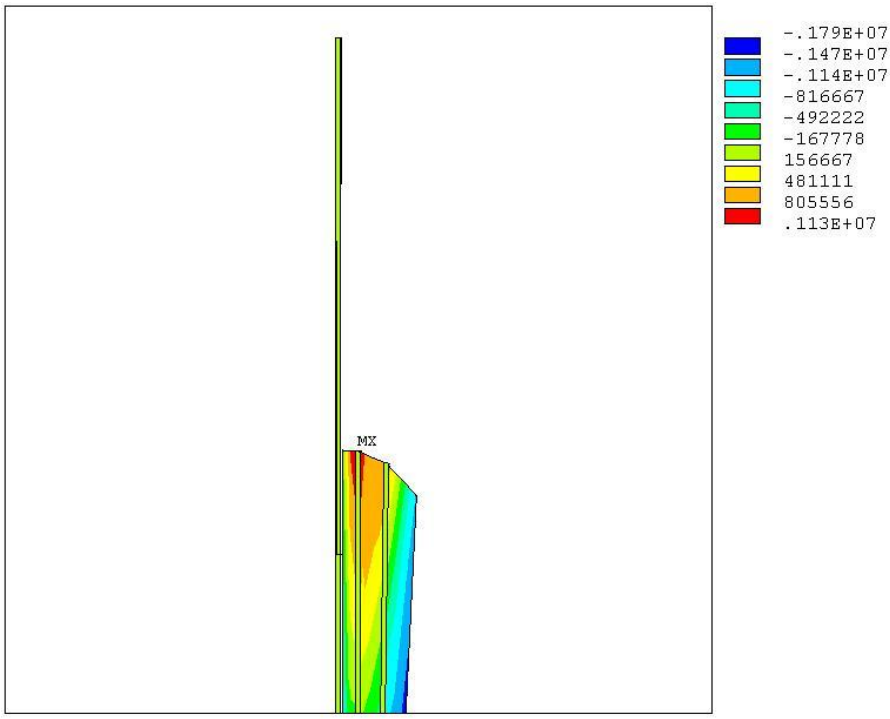


*Figure 6.10: The y-components of stress at the top of the well for case 1 [Pa].*

If the stresses in the figure are examined for the cement between the production casing and the anchor casing, it can be seen that the stresses are compressive along the production casing but tensile along the anchor casing. This can be explained by the pressure loads inside the well that causes the compressive y-components of stresses in the cement.

The maximum y-components of tensile stress for the cement in the model is 1.17 MPa at the top of the cement located between the production casing and the anchor casing, but the maximum compressive stress is only at a very small section at the bottom of the cement. The von Mises stresses are below the yield stress of the cement at all points, defined as 2.43 MPa in tension and 24.3 MPa in compression, except for the compressive stress peak at the bottom of the cement. The maximum compressive stress at the peak is 117 MPa, but this stress magnitude is probably too high because the material properties of the cement are modeled linear. The compression stress ranges over the cement's ultimate compressive stress defined as 26 MPa in the model, which would cause the cement to break at the bottom. When the well is modeled with nonlinear material properties, the solution does not converge for the cement, since the model can not simulate the breaking of the cement. So it is likely that the

compressive stress exceeds the ultimate stress of the cement at the bottom due to the weight of the cement, but it is unlikely that the maximum stresses are as high as the model's result imply.

For comparison, the stresses were examined for case 4, where the friction coefficient and the maximum friction stress are defined so high that the production casing is almost fixed to the cement. The highest von Mises stresses of the pipes are above the completely fixed part of the production casing, ranging from the depth of 150 m up to 45 m. The maximum stress of the pipes is 343 MPa so it does not reach the yield stress of the steel.

The maximum y-component of the compressive stress resulting from the model is 119 MPa at the part of the cement fixed to the production pipe and the maximum y-component of the tensile strength is 6.30 MPa at the top of the cement. The y-components of the stresses for the cement reach the ultimate strength both in compression and tension, so the cement is likely to break. However, as for the case case having contact elements with lower friction coefficient and maximum friction stress, the high compressive stress resulting from the model is probably higher than in reality since linear material properties are used to model the well. Table 6.8 rounds up the maximum stresses for those two cases.

*Table 6.8:* Comparison of the stresses based on the connection between the production casing and the cement.

| Connection between steel and cement | Maximum von Mises stress of steel [MPa] | Maximum y-component tensile stress of cement [MPa] |
|---|---|---|
| Case 1: Contact elements, and fixed from 150 m to 550 m: | 334 | 1.17 |
| Case 4: High friction, and fixed from 150 m to 550 m: | 343 | 6.30 |

The definition of the connection behavior between the steel and the cement affects the results for the y-components of the tensile stresses. The case that is almost fixed everywhere, results in much higher y-components of the tensile stresses. When the casing is fixed to the cement, the cement undergoes high forces because the thermal expansion of the casing is more than the expansion of the cement.

### 6.3.3 Comparison Based on Different Young's Modulus of Cement

The Young's modulus of the cement is defined as $2.79 \cdot 10^9$ Pa in section 6.1, but a Young's modulus of $4 \cdot 10^9$ Pa is also modeled in order to estimate its effect on the results. The casing

is fixed from 150 m to 550 m as for case 1 and the displacement results are the same as for that case, but the y-components of the stresses are different, as shown in Table 6.9.

*Table 6.9:* Comparison of the stresses based on the Young's modulus of the cement.

| Young's modulus [GPa] | Maximum von Mises stress of steel [MPa] | Maximum y-component compressive stress of cement [MPa] | Maximum y-component tensile stress of cement [MPa] | Maximum y-component tensile strain of cement |
|---|---|---|---|---|
| E = 2.79 | 334 | 117 | 1.17 | $0.551 \cdot 10^{-3}$ |
| E = 4.00 | 333 | 120 | 1.50 | $0.280 \cdot 10^{-3}$ |

The compressive and tensile y-components of the stresses are higher for the case with Young's modulus of $4 \cdot 10^9$ Pa. The y-components of the tensile strains are lower for the higher value of Young's modulus, as expected, since the difference in maximum tensile stresses is not high when the Young's modulus is considerably increased.

It can be difficult to choose the right constraints for the model because the the connection behavior between the steel and the cement in reality is not necessarily known. The model is, however, useful to estimate the the effect of different parameters and constraints, when the well is designed.

## 6.4 Three Dimensional Buckling Analysis

The three dimensional buckling model can be used to examine the buckling strength of the production casing as well as the corresponding buckled mode shape. Nonlinear analysis formulation is used in this case study, but both linear and nonlinear buckling formulations are described in section 3.3. First, a structural analysis is performed to estimate the rising of the production casing for the well defined in section 6.1, in order to compare the results to the results from the 2d model. Due to the enormous size of the model in three dimensions, the well was only modeled down to 160 m and the radius of the formation modeled was 35 cm. Recall that the depth of the well is 2300 m. Displacements from the 2d structural model were used as constraints on the outer surface of the formation, to simulate the formation's real behavior. The displacement constraints were also used on the bottom of the well to simulate loads due to the weight of the well. There is only a 1 m section of the pipe defined with contact elements at the depth of 152 m, but the production casing is merged to the cement everywhere else. Figure 6.11 shows the y-displacement in the part of the well modeled.

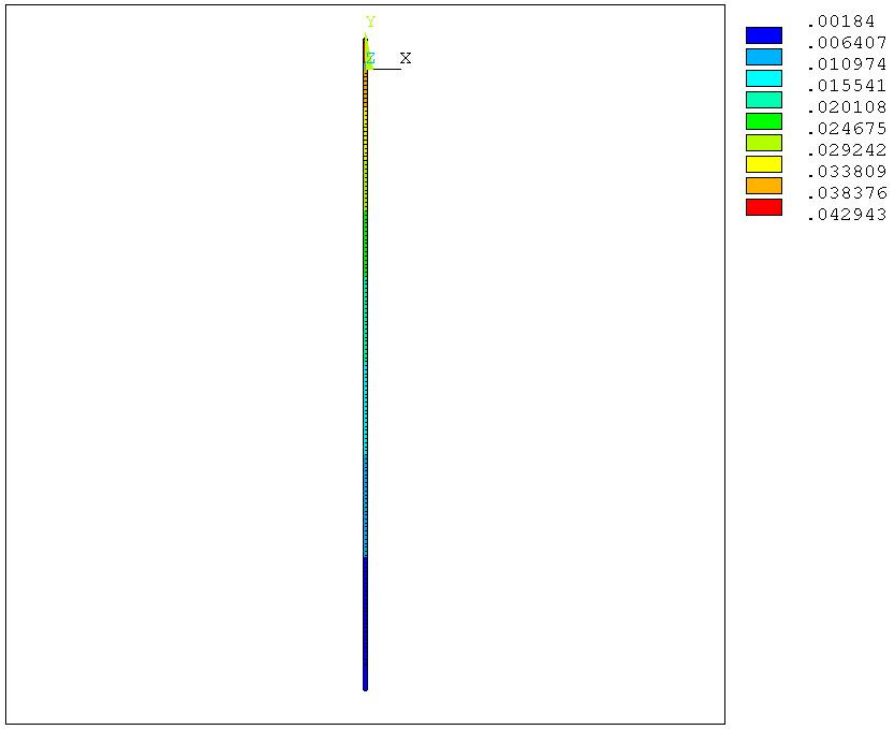


*Figure 6.11: Displacement of the well in y direction [m].*

The maximum displacement at the top of the well is 0.0429 m as shown in Table 6.10.

*Table 6.10:* Comparison of the displacement between the 3d model and the 2d model.

| Model | Maximum upward displacement at the top [m] |
|---|---|
| 3d model: | 0.0429 |
| 2d model, case 4: | 0.0434 |

The table shows for comparison, the maximum displacement for case 4 analyzed with the 2d model where the friction coefficient and the maximum friction stress were defined to be so high that the production casing was almost fixed to the cement. In the 3d analysis, the production casing is fixed to the cement, so the results for the two cases should be similar, as

shown in the table. It is therefore likely that the displacement constraints, transferred from the two dimensional model, are simulating the well's behavior correctly, based on the 2d analysis.

In the buckling analysis of the well, a 20 MPa sideward pressure is defined at a small area at the depth ranging from 152.4 m to 152.6 m, where the contact elements exist (there are contact elements between 152 - 153 m), since buckling does not occur for the loads predefined. The area is 0.0113 $m^2$ and the location is shown in Figure 6.12.

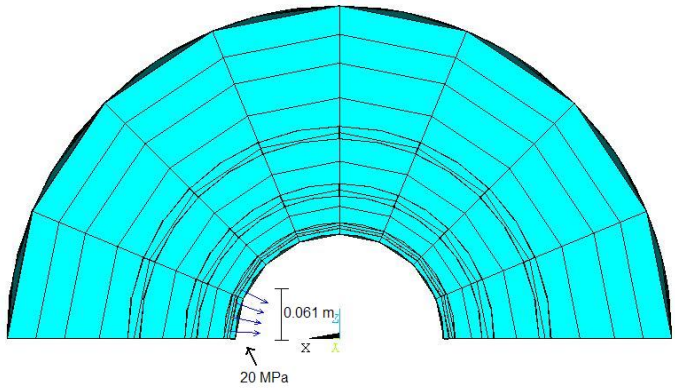


*Figure 6.12: The location of the 20 MPa sideward pressure.*

The sideward pressure is modeled to simulate the buckling strength if fluid is trapped outside the production casing and its thermal expansion causes sideward pressure acting on the casing. The sideward pressure could also be due to pressure and temperature changes inside the well when the water in the well boils.

The buckling occurs at a time step of 0.853 so 85.3% of the loads acting on the well would cause the well to buckle. A load magnitude of that size might probably be present at a geothermal well if fluid trapped in the cement expands causing a sideward pressure to act on the production casing. Figure 6.13 shows the buckled mode shape of the well, where the displacements are magnified by 100% to amplify the shape.

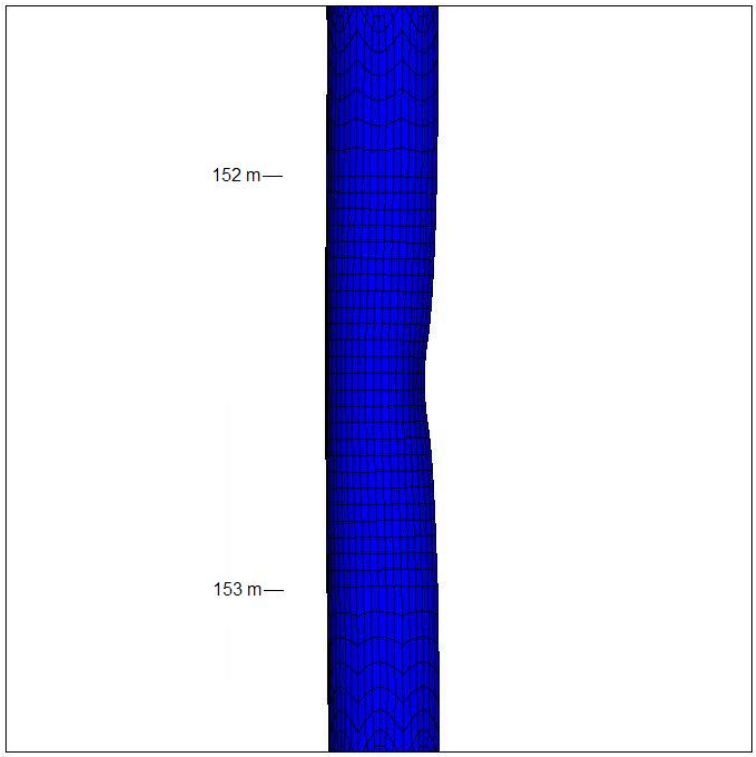


*Figure 6.13: The buckled mode shape of the well (displacements magnified by 100%).*

The well buckles inward as shown clearly in Figure 6.14.

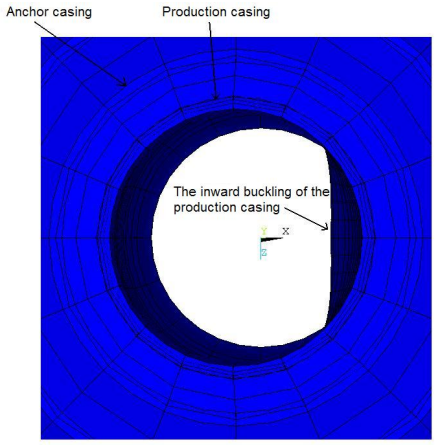


*Figure 6.14: The buckled mode shape of the well, top view (displacements magnified by 100%).*

There have been some examples of buckling in geothermal wells at different depths. Figure 6.15 shows for example a collapsed 9 5/8" production casing at a depth of 73.5 m, where the shape is in some way similar to the buckled mode shape resulting from the model.

*Figure 6.15: A casing failure of a real geothermal well [Thorallsson, 2008].*

The casing buckles inward as for the buckling shape resulting from the model. The maximum von Mises stress is shown in Figure 6.16.

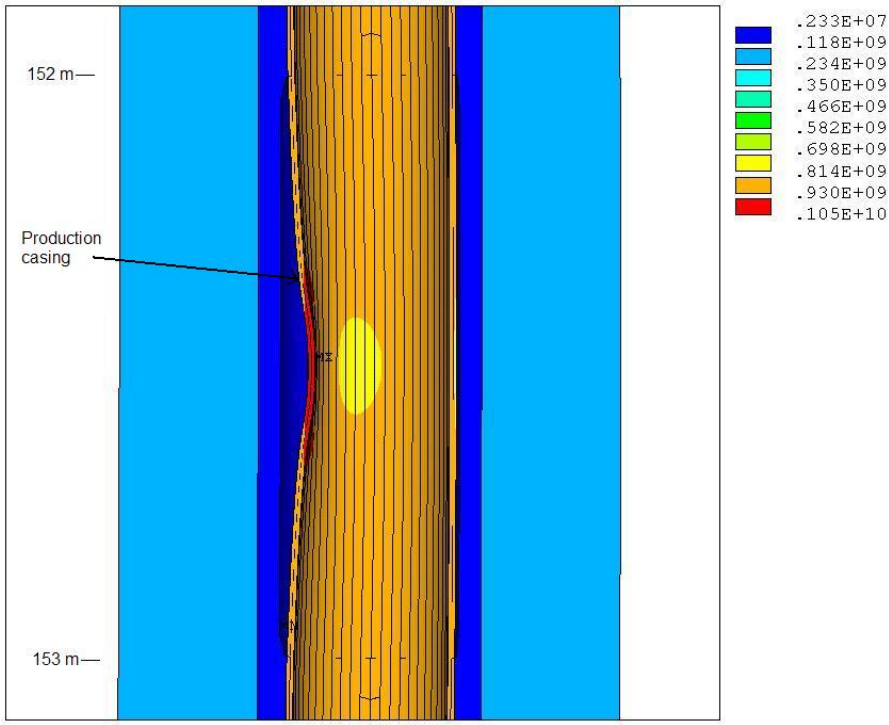


*Figure 6.16: The von Mises stresses at the buckling location [Pa].*

The maximum stress is 1.05 GPa, at the location where the well buckles. Figure 6.17 shows the displacements in x direction.

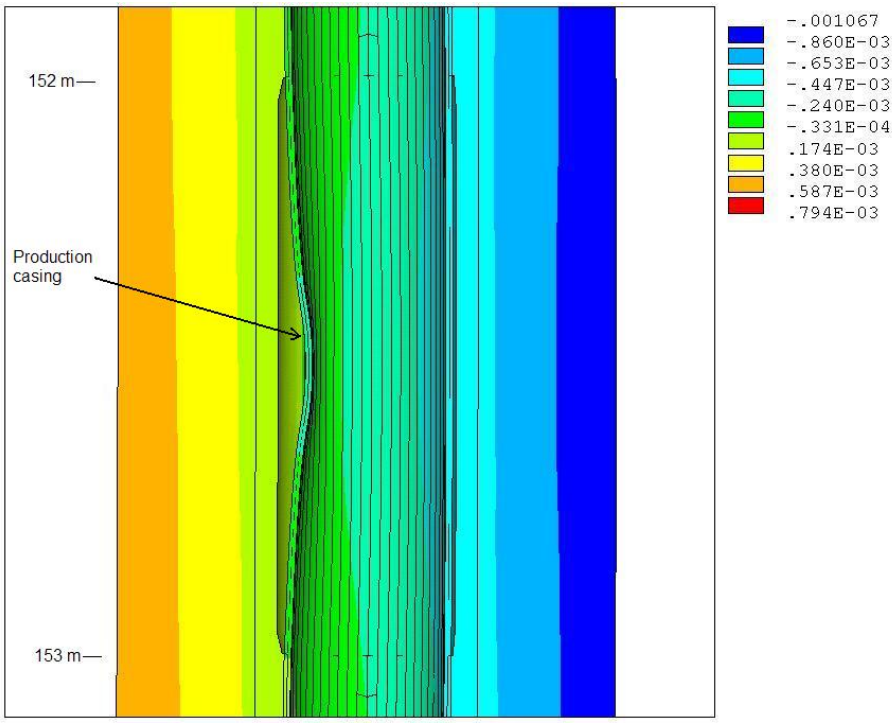


*Figure 6.17: The x-displacements where the well buckles [m].*

The x displacement where the buckling occurs is between -0.447·10$^{-3}$ m and -0.240·10$^{-3}$ m. The displacement to the right is negative since the same coordinate system is used as in Figure 6.12.

The area at which the sideward pressure is acting on the production casing can be variable in size. The size was therefore increased from 0.011 m$^2$ to 0.045 m$^2$ in order to examine its effect on the buckling strength. Figure 6.18 shows the location of the increased area where the sideward pressure is defined.

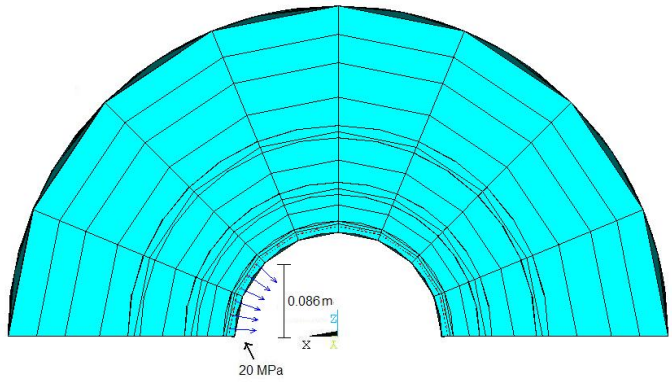


*Figure 6.18: The location of the 20 MPa sideward pressure acting on an increased area.*

The vertical size of the area is 0.6 m instead of 0.2 m before, and the depth is ranging from 152.2 m to 152.8 m. Even though the area is expanded, the buckling occurs at the same time step, or 0.853. Increasing the area does therefore not affect the load magnitude causing the well to buckle. The displacements at the buckling location are though larger, as shown in Figure 6.19.

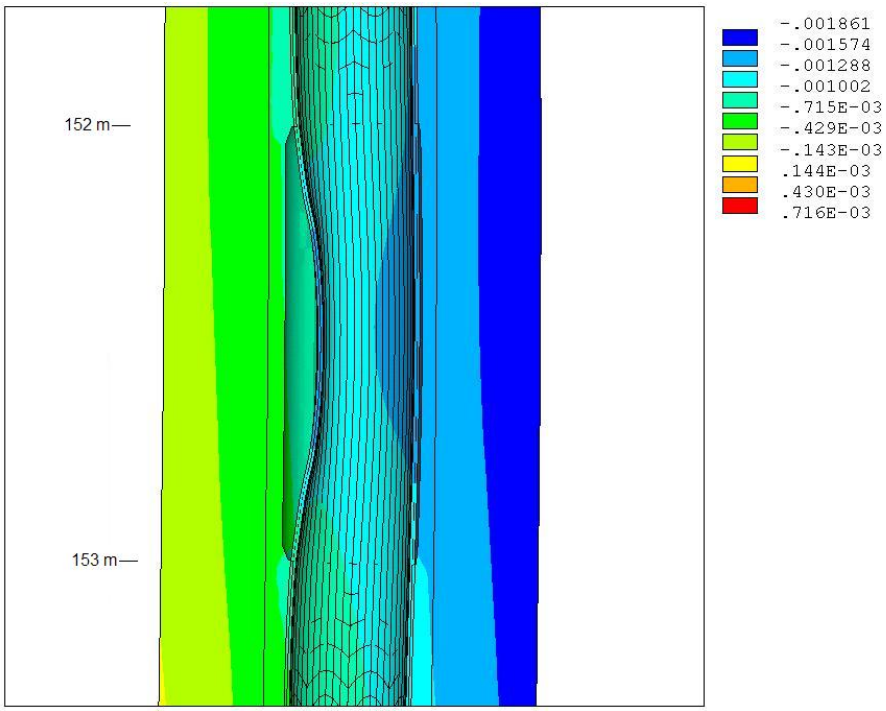


*Figure 6.19: The x-displacements where the well buckles for an increased sideward pressure area [m].*

The displacement where the buckling occurs is between -1.574·$10^{-3}$ m and -1.288·$10^{-3}$ m so the displacement is considerably larger if the area is increased, as can be seen if Figure 6.19 is compared to Figure 6.17. Table 6.11 rounds up the displacements at the buckling location, for the two different sizes of sideward pressure areas.

*Table 6.11:* Comparison of the displacements for two different sizes of sideward pressure areas.

| Sideward pressure area [$m^2$] | Displacements interval [m] |
|---|---|
| 0.011 | -0.447·$10^{-3}$ to -0.240·$10^{-3}$ |
| 0.045 | -1.574·$10^{-3}$ to -1.288·$10^{-3}$ |

The model shows an inward buckling of the production casing, where the buckling shape is similar to a buckling case of a real geothermal well, when a 20 MPa sideward pressure is

acting on the production casing. The same load caused the well to buckle though the sideward pressure area was increased, but the displacements were larger for the increased area. The loads accounted for in this buckling analysis are load magnitudes that might be present in real geothermal wells, so buckling is not unlikely to occur in those wells, according to the model. Since the model is parametrical, it could be useful to estimate whether changing some other parameters when designing the well would result in decreased risk of failure due to buckling.

# 7 Conclusions

The focus of this study was to develop three types of complete finite element models that can assist with the designing of geothermal wells. Studies have shown the importance of designing the wells not only based on the compressive strength of the materials, but also on the stress fields, nonuniform loadings and the interactions between the cement and the steel.

First, a two dimensional thermal analysis was performed in order to examine the temperature distribution of the well. Three casings, cement around them, a production liner and the surrounding formation were modeled. The temperature results are based on a predefined temperature distributions inside the well and for the ground around it where it is not affected by the well's temperature. The temperature results are then used as loads for two other models, a two dimensional structural analysis and a three dimensional buckling analysis.

The 2d structural model is used to simulate the expansion and the stresses of the well due to the temperature loads as well as gravity and pressure inside the well. The effects of different connections between the steel and the cement can also be examined, by defining the behavior of contact elements that are used to model the connection. The von Mises stresses resulting from the simulation are useful in order to estimate whether plastic deformation occurs, by comparing them to the materials' yield strength.

Finally, the 3d buckling analysis is useful to study the buckling behavior of the well's innermost casing. The same loads as in the 2d structural model are used and the entire well can be modeled. A sideward pressure is also modeled, to simulate the buckling strength if fluid is trapped outside the production casing and its thermal expansion causes sideward pressure on the casing. The sideward pressure could also be due to pressure changes inside the well when the water inside boils. There are some possibilities available in the model in order to reduce the computer solving time due to the enormous size of the model. The ground is for example modeled smaller and the well can be modeled only down to some specific depth.

The real behavior of the well is then simulated by using displacement constraints from the two dimensional analysis on the outer surface of the ground and on the bottom of the well if the entire well is not modeled. There is also a possibility to have only contact elements on a small part of the well, where buckling will then occur.

In the case study of the project, a 2300 m deep geothermal well is modeled. The production casing of the well is 9 5/8 inches and the casings are made out of K55 carbon steel. The temperature distribution resulting from the thermal model shows a rising in the temperature along the production pipe due to thermal conduction from the water inside the well. The 2d structural model is used to model wells with different contact behavior between the steel in the production pipe and the cement, and it shows how the connection behavior greatly affects the results. The upward displacement results of the production pipe for the connection behavior assumed in a real well are close to the results for a well with the cement completely fixed to the production pipe. The maximum upward displacement is at the top of the production pipe, 0.0468 m. The results for no connection between the cement and the steel are considerably higher. The von Mises stresses of the casings do not range over the yield stress of the steel but the compressive y-component stress of the cement reaches over the cement's ultimate strength. When the Young's modulus of the cement is increased, the tensile strain becomes larger but the stresses do not change much. The study shows how the connection behavior defined between the cement and the steel greatly affects the results, so it is important to choose it carefully. But even though the real connection behavior of a geothermal well can not be defined, the model can be useful to estimate the effect of different parameters and constraints of the well.

The 3d buckling model is used to estimate the rising of the production casing where the well is modeled down to 160 m in order to compare the results to the 2d analysis. The results were almost the same as from the 2d analysis when the casing is fixed to the cement, as modeled in the 3d model. The buckling strength was also examined for two different cases, i.e. when a 20 MPa sideward pressure is acting on two different sizes of areas on the production casing. The same load magnitude caused the well to buckle for the two cases, or 85.3% of the loads defined in the model. The displacements were though larger when the sideward pressure area was increased. The loads accounted for in the buckling analysis of this case study are load magnitudes that might be present in real geothermal wells, so buckling is not unlikely to occur in those wells, according to the model. The model could be useful to estimate whether changing some other parameters when designing the well would result in decreased risk of failure due to buckling.

Many improvements could be made to the 2d and 3d models in the future. Bringing in the effect of corrosion in the pipes is for example a very interesting possibility and a user interface could be developed to ease the use of the model. Another interesting option is to use the three dimensional model to model directionally drilled wells.

# A Evaluation of the Interfacial Shear Force between the Steel Casing and the Cement

The push-out tests that were performed in cooperation with ICI Rheocenter at Innovation Center Iceland, are experimental techniques widely used to evaluate shear stiffness and shear strength of two materials' interface strength. The push out setup in the experiment, was developed at the University of Iceland faculty of engineering, in connection to the M.Sc. thesis of Sif Gretarsdottir [Gretarsdottir, 2007], where Vilhjalmur Sigurjonsson, technician at the faculty of engineering, constructed the molds, designed the test setup and executed the push out experiments. The push out test was supervised by Sunna O. Wallevik, chemist at ICI Rheocenter, and Bjorn Hjartarson, industrial engineer at ICI Rheocenter. The experiments were carried out in a press of type Instron (load cell type: 8503), which is an uniaxial press, located at University of Iceland. The mixing of the slurry mixes were carried out by Sunna O. Wallevik and Stefan Kubens, building engineer at ICI Rheocenter.

The special molds, made by Vilhjalmur for Sif's thesis, were reused for this test but some additional molds for the test were constructed at ICI Rheocenter. A close up shot of the molds can be seen in Figure A.1.

*Figure A.1: Close up shots of the molds.*

The molds were made of water proof plywood and could be disassembled into three individual parts, the base plate (cm x cm square), top plate (cm x cm square with a centered circular hole of x cm) which is fastened to the base plate with 4 stainless steel bolts and x cm circular plate which is fastened to the base plate with a stainless steel bolt. A 0.8 mm galvanized steel sheet was put inside each plywood mold and its sole purpose is to serve as the inner wall of the anchor casing. This material was chosen because of its neutrality against the concrete. Because the plywood has been cut there is a chance it might draw some of the water out of the concrete hence altering its combination and therefore the material properties of the hardened concrete.

The circular plate is fastened onto the center of the base plate. The external diameter of the circular plate is the same as the internal diameter of the steel casing. The steel casing is placed into the mold and fastened around the circular plate. At last the galvanized steel sheet is bent into a circle so it will fit into the circular cut in the top plate. A small plywood chip is used to make sure the steel sheets stays in a circular shape, as seen in Figure A.1.

The steel casings used in the experiment were 18 cm (7 in) in external diameter, 8 mm thick, and made of K-55 steel. The casings were cut into 5 cm high samples which all were planed in a turning lathe in a local machine shop. The external surface of the casings was glassblasted in order to ensure the same surface properties independent of which sample was used for different type of slurry mix. The surface of the casing was very rusty (had been standing outside the machine shop for more then 1 year) but according to specialists in this

field the casing are often covered in oil slick/tare when delivered from the fabric in Russia. This slick is both from the factory and is also lubricated on purpose to prevent the casings from rusting during transportation to Iceland.

After the slurry had been mixed at the laboratory of ICI Rheocenter (mixed in a Hobart mixer as described in the ASTM C-305 standard) the slurry was casted in the flange between the steel casing and the metal sheet, see Figure A.2.

*Figure A.2: The slurry placed in the molds.*

After the slurry had been casted in the flanges between the steel casing and the steel sheet, a plastic bag was put over the mold and closed tightly in order to prevent any moisture to escape. A plastic cup full of water was place into each mold to to ensure moist environment inside the bag hence preventing shrinkage in the hardened concrete. If this is not done the concrete would most likely start to crack during the hardening period.

10 specimens were made for each mix, five for 1 day push out test and five for 28 day push out test. The push out tests were done after one day and 28 days respectively. One day's strength of the slurry is of interest since it shows the most critical strength development with regards to reduction in WOC time. The 28 day's strength is almost 100% of the final strength

the slurry reaches.

When the samples had been taken out of the mold (demolded) and the thin steel sheet removed, the samples were placed in a press of type Instron as mentioned earlier. A special test setup was built to place the sample correctly into the press. The casing is placed between the top steel plate and the steel ring as displayed in Figure A.3.

*Figure A.3: Casing placed between the top steel plate and the steel ring.*

The thick circular steel plate had eight bolts through it. When the press reached the start position, the bolts were tightened. The bolts were used to adjust the circular steel plate so that the pressure exerted would be exactly perpendicular on the sample. This was necessary to insure that the top of the sample was always in plane with the press surface. The whole test setup can be seen in Figure A.4.

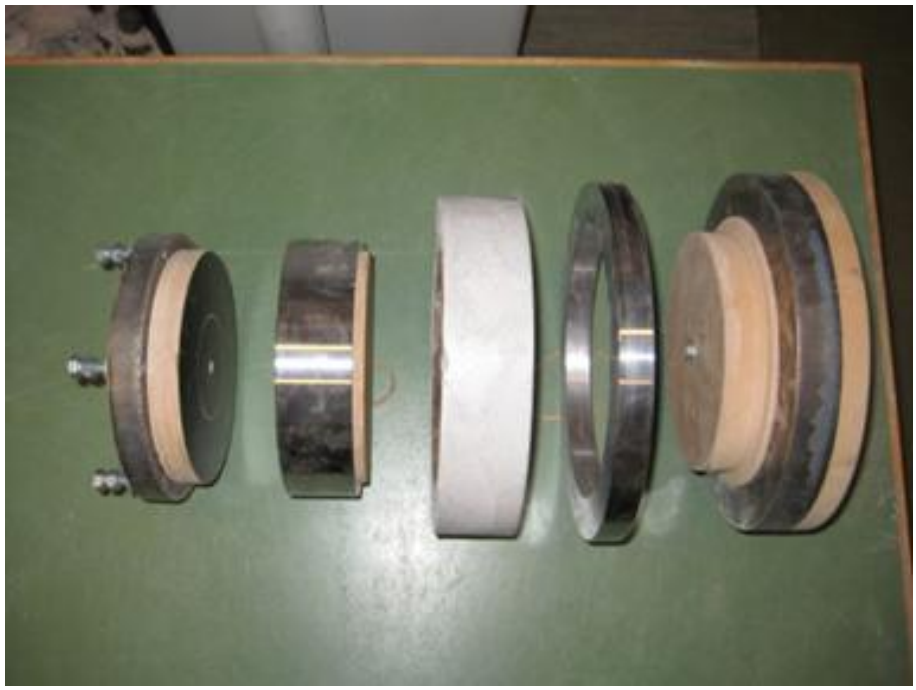

*Figure A.4: The whole test setup.*

Two different mixes were tested in those experiments. Mix A consists of the mix design of the conventional concrete slurry mix which has been used in Iceland for over 40 years with very minor changes. This mix includes 2 % of expanded pearlstone (Europearl), which is a low density material. Mix B consists of the same mix design as Mix A except the Europearl has been replaced with Liaver-micro glassballs (20% of cement weight). The advantage of the Liaver-micro glassballs is that they can be used in much higher dosage compared to the Europearl since they are better distributed in the concrete mix. Another important advantages of the Liaver material are high compressive strength and low thermal conductivity. Both there properties are very important in concrete slurry for geothermal wells.

Table displays the test results from the push out test. The 1 day interfacial shear strength for the 1 day old concrete is almost the same for both mixes. The 28 day interfacial shear strength is however slightly higher for Mix A.

*Table A.1:* The results from the push-out test.

| 1 day | 28 days | Shear strength [MPa] |
|---|---|---|
| Mix A | 0.19 | 0.72 |
| Mix B | 0.18 | 0.65 |

Based on these test results it was decided to use the interfacial shear strength results for Mix A as the value for the computer simulation of the geothermal well.

# Bibliography


Gudni Axelsson, February 2009. An interview with Gudni Axelsson from ISOR (Iceland GeoSurvey), *Gudni.Axelsson@isor.is*.

Ted Belytschoko, Wing Kam Liu, and Brian Moran. *Nonlinear Finite Elements for Continua and Structures*. John Wiley & Sons Ltd., 2000.

G. Björnsson and A. Hjartarson. Technical report, Íslenskar orkurannsóknir (Iceland GeoSurvey), 2003. Reiknilíkan af jarðhitakerfum í Hengli og spár um framtíðarástand við allt að 120 MW rafmagnsframleiðslu á Hellisheiði og 120 MW á Nesjavöllum.

Nikolas I. Christensen. Poisson's ratio and crustal seismology. *Journal of Geophysical Research Solid Earth*, 101:Pages 3139 – 3156, 1995.

Gene Culver. *Geothermal Direct Use Engineering and Design Guidebook*. Geo-Heat Center, Oregon Institute of Technology, 2005. Chapter 6.

Mary H. Dickson and Mario Fanelli. *Geothermal Energy, Utilization and Technology*. Earthscan, 2005. Utilization and Technology.

Encyclopædia Britannica. Online, 9. April 2009, 2009. *http://www.britannica.com/EBchecked/topic/505970/rock*.

W.W. Fleckenstein, A.W. Eustes, W.J. Rodriguez, Andreas Berger, and Francisco J. Sanchez. Cemented Casing: The True Stress Picture. 2005. Paper AADE-05-NTCE-14 presented at the AADE 2005 National Technical Conference and Exhibition, Houston, Texas, April 5-7.

Sif Gretarsdottir, 2007. Mechanical and thermal properties of well cement, a Master of Science thesis.

Olafur H., February 2009. An interview with Olafur H. Wallevik from the Innovation Center Iceland, *olafur.w@nmi.is*.

T.J. Hammons. Geothermal power generation: global perspectives; U.S.A. and Iceland; Technolgoy, direct uses, plants, and drilling. *Interantional Journal of Power and Energy Systems*, 203, 2007.

Haukur Jóhannesson and Kristján Sæmundsson, 2002. Geothermal map of Iceland.

Martin Kaltschmitt, Wolfgang Streicher, and Andreas Wiese. *Renewable Energy, Technology, and Environment Economics.* Springer Berlin Heidelberg, 2007.

Sigrun Nanna Karlsdottir, Oktober 2008. An interview with Sigrun Nanna Karlsdottir from the Innovation Center Iceland, *SigrunKarls@nmi.is*.

Cheng Yu Li and Barzin Mobashert. Finite Element Simulations of Fiber Pullout Toughening in Fiber Reinforced Cement Based Composites. *Elsevier Science Ltd.*, 7:Pages 123 – 132, 1998.

John W. Lund, Derek H. Freeston, and Tonya L. Boyd. Direct applicaton of geothermal energy: 2005 Worldwide review. *Geothermics*, 34:Pages 691 – 727, 2005.

Karol Miller, Grand Joldes, Dane Lance, and Adam Wittek. Total Lagrangian explicit dynamics finite element alogrithm for computing soft tissue deformation. *Commun. Numer. Meth. Engng*, 23:Pages 121 – 134, 2007.

Orkustofnun. Webpage, 2007. Energy Statistic in Iceland, *http* : *//www.os.is/Apps/WebObjects/Orkustofnun.woa/swdocument/*20644*/Energystatistics*2007*.pdf*.

Orkuveita Reykjavíkur. Webpage. Energy and Environment, Geothermal, *http* : *//www.or.is/English/EnergyandEnvironment/Geothermal/*.

Orkuveita Reykjavíkur. Webpage, 2003. Nesjavellir Power Plant, *http* : *//www.or.is/media/PDF/nesjavellir*$_e$*ng.pdf*.

A.J. Philippacopoulos and M.L. Berndt. Characterization and modeling of cements for geothermal well casing remediation. *Geothermal Resources Council Transactions*, 24: Pages 81–86, 2000.

Aristodimos J. Philippacopoulos and Marita L. Berndt. Structural analysis of geothermal well cements. *Geothermics*, 31:Pages 657 – 676, 2002.

Walter D. Pilkey and Walter Wunderlich. *Mechanics of Structures*. CRC Press, Inc., 1994. Variational and Computational Methods.

Robert P. Rechard and Karl W. Schuler. Report prepared by Sandia National Laboratories for the United States Department of Energy., February 1983. Euler Buckling of Geothremal Well Casing.

Glitnir Geothermal Energy Research. webpage, March 2008. Geothermal energy, The only real base-load capacity alternative of the renewables, *http* : *//www.glitnirbank.com/servlet/file/FactSheet*$_G$*eothermalEnergy.pdf*.

Inc. SAS IP. Ansys Manual, 2007. Vers. 11.0.

Mehdi Abbaszadeh Shahri, December 2005. Detecting and modeling cement failure in high pressure/high temperature wells, using finite-element method.

Ómar Sigurðsson and Einar Gunnlaugsson. Prepared for Hitaveita Reykjavíkur., Mars 1989. Nesjavellir hola NJ-18.

James N. A. Southon. Proceedings World Geothermal Congress, Antalya, Turkey, April 2005. Geothermal Well Design, Construction and Failures.

Sverrir Thorallsson. Gothermal Boreholes - lecture notes, January 2008. Lecture notes in the course 08.23.70 Geothermal Power Development at the University of Iceland.

J. Wu, M.E. Gonzalez, and N. Hosn. Steam Injection Casing Design. 2005. Paper prepared for presentation at the 2005 SPE Western Regional Meeting held in Irvine, CA, U.S.A, March 30 - April 1 2005.

O. C. Zienkiewicz. *The Finite Element Method*. McGras-Hill Book Company (UK), 1977. Third Edition.